(Article begins on next page)

01/05/2026 00:40

EUROPEAN ORGANIZATION FOR NUCLEAR RESEARCH

CERN–EP/2001–067
20.09.2001

A precise measurement of the direct CP violation parameter $\mathrm{Re}(\varepsilon'/\varepsilon)$

NA48 Collaboration

A. Lai, D. Marras
Dipartimento di Fisica dell'Università e Sezione dell'INFN di Cagliari, I-09100 Cagliari, Italy.

A. Bevan[1)], R.S. Dosanjh, T.J. Gershon[2)], B. Hay[3)], G.E. Kalmus, C. Lazzeroni, D.J. Munday, M.D. Needham[4)], E. Olaiya, M.A. Parker, T.O. White, S.A. Wotton
Cavendish Laboratory, University of Cambridge, Cambridge, CB3 0HE, U.K.[5)].

G. Barr, G. Bocquet, A. Ceccucci, T. Cuhadar-Dönszelmann, D. Cundy, G. D'Agostini, N. Doble, V. Falaleev, W. Funk, L. Gatignon, A. Gonidec, B. Gorini, G. Govi, P. Grafström, W. Kubischta, A. Lacourt, M. Lenti[6)], S. Luitz[7)], J.P. Matheys, I. Mikulec[8)], A. Norton, S. Palestini, B. Panzer-Steindel, D. Schinzel, G. Tatishvili[9)], H. Taureg, M. Velasco, O. Vossnack, H. Wahl
CERN, CH-1211 Genève 23, Switzerland.

C. Cheshkov, A. Gaponenko[10)], P. Hristov, V. Kekelidze, D. Madigojine, N. Molokanova, Yu. Potrebenikov, A. Tkatchev, A. Zinchenko
Joint Institute for Nuclear Research, Dubna, Russian Federation.

I. Knowles, V. Martin, H. Parsons, R. Sacco, A. Walker
Department of Physics and Astronomy, University of Edinburgh, Edinburgh, EH9 3JZ, U.K.[5)].

M. Contalbrigo, P. Dalpiaz, J. Duclos, P.L. Frabetti[11)], A. Gianoli, M. Martini, F. Petrucci, M. Savrié, M. Scarpa
Dipartimento di Fisica dell'Università e Sezione dell'INFN di Ferrara, I-44100 Ferrara, Italy.

A. Bizzeti[12)], M. Calvetti, G. Collazuol, G. Graziani, E. Iacopini, F. Martelli[13)], M. Veltri[13)]
Dipartimento di Fisica dell'Università e Sezione dell'INFN di Firenze, I-50125 Firenze, Italy.

H.G. Becker, H. Blümer, D. Coward, M. Eppard, H. Fox, A. Hirstius, K. Holtz, A. Kalter, K. Kleinknecht, U. Koch, L. Köpke, P. Lopes da Silva, P. Marouelli, I. Pellmann, A. Peters, S.A. Schmidt, V. Schönharting, Y. Schué, R. Wanke, A. Winhart, M. Wittgen
Institut für Physik, Universität Mainz, D-55099 Mainz, Germany[14)].

J.C. Chollet, S. Crépé, L. Fayard, L. Iconomidou-Fayard, J. Ocariz, G. Unal, I. Wingerter-Seez
Laboratoire de l'Accélérateur Linéaire, IN2P3-CNRS,Université de Paris-Sud, 91898 Orsay, France[15)].

G. Anzivino, P. Cenci, E. Imbergamo, P. Lubrano, A. Mestvirishvili, A. Nappi, M. Pepe, M. Piccini
Dipartimento di Fisica dell'Università e Sezione dell'INFN di Perugia, I-06100 Perugia, Italy.

L. Bertanza, P. Calafiura, R. Carosi, R. Casali, C. Cerri, M. Cirilli[16)], F. Costantini, R. Fantechi, S. Giudici, I. Mannelli, V. Marzulli, G. Pierazzini, M. Sozzi
Dipartimento di Fisica, Scuola Normale Superiore e SezioneINFN di Pisa, I-56100 Pisa, Italy.

J.B. Cheze, J. Cogan, M. De Beer, P. Debu, F. Derue, A. Formica, R. Granier de Cassagnac, E. Mazzucato, B. Peyaud, R. Turlay, B. Vallage
DSM/DAPNIA - CEA Saclay, F-91191 Gif-sur-Yvette, France.

I. Augustin, M. Bender, M. Holder, A. Maier, M. Ziolkowski
Fachbereich Physik, Universität Siegen, D-57068 Siegen, Germany[17)].

R. Arcidiacono, C. Biino, N. Cartiglia, R. Guida, F. Marchetto, E. Menichetti, N. Pastrone
Dipartimento di Fisica Sperimentale dell'Università e Sezione dell'INFN di Torino, I-10125 Torino, Italy.

J. Nassalski, E. Rondio, M. Szleper, W. Wislicki, S. Wronka
Soltan Institute for Nuclear Studies, Laboratory for High Energy Physics, PL-00-681 Warsaw, Poland[18)].

H. Dibon, G. Fischer, M. Jeitler, M. Markytan, G. Neuhofer, M. Pernicka, A. Taurok, L. Widhalm
Österreichische Akademie der Wissenschaften, Institut für Hochenergiephysik, A-1050 Wien, Austria[19)].

Submitted to European Physical Journal

Abstract

The direct CP violation parameter $\mathrm{Re}(\varepsilon'/\varepsilon)$ has been measured from the decay rates of neutral kaons into two pions using the NA48 detector at the CERN SPS. With 3.3 million $K_L \to \pi^0\pi^0$ events collected during the 1998 and 1999 running periods, a result of $\mathrm{Re}(\varepsilon'/\varepsilon) = (15.0 \pm 2.7)\times 10^{-4}$ has been obtained. The result combined with the published 1997 sample is $\mathrm{Re}(\varepsilon'/\varepsilon) = (15.3 \pm 2.6)\times 10^{-4}$.

[1)] Present address: Oliver Lodge Laboratory, University of Liverpool, Liverpool L69 7ZE, U.K.

[2)] Present address: High Energy Accelerator Research Organization (KEK), Tsukuba, Ibaraki, 305-0801, Japan.

[3)] Present address: EP Division, CERN, 1211 Genève 23, Switzerland.

[4)] Present address: NIKHEF, PO Box 41882, 1009 DB Amsterdam, The Netherlands.

[5)] Funded by the U.K. Particle Physics and Astronomy Research Council.

[6)] On leave from Sezione dell'INFN di Firenze, I-50125 Firenze, Italy.

[7] Present address: SLAC, Stanford, CA., 94309, USA.
[8] On leave from Österreichische Akademie der Wissenschaften, Institut für Hochenergiephysik, A-1050 Wien, Austria.
[9] On leave from Joint Institute for Nuclear Research, Dubna, 141980, Russian Federation.
[10] Present address: University of Alberta, Edmonton Alberta T6G 2J1, Canada.
[11] Dipartimento di Fisica e INFN Bologna, viale Berti-Pichat 6/2, I-40127 Bologna, Italy.
[12] Dipartimento di Fisica dell'Universita' di Modena e Reggio Emilia, via G. Campi 213/A I-41100, Modena, Italy.
[13] Instituto di Fisica Universitá di Urbino
[14] Funded by the German Federal Minister for Research and Technology (BMBF) under contract 7MZ18P(4)-TP2.
[15] Funded by Institut National de Physique des Particules et de Physique Nucléaire (IN2P3), France
[16] Present address: Dipartimento di Fisica dell'Universitá di Roma "La Sapienza" e Sezione INFN di Roma, I-00185 Roma, Italy.
[17] Funded by the German Federal Minister for Research and Technology (BMBF) under contract 056SI74.
[18] Supported by the Committee for Scientific Research grants 5P03B10120, 2P03B11719 and SPUB-M/CERN/P03/DZ210/2000 and using computing resources of the Interdisciplinary Center for Mathematical and Computational Modelling of the University of Warsaw.
[19] Funded by the Austrian Ministry of Education, Science and Culture under contract GZ 616.360/2-IV GZ 616.363/2-VIII, and by the Fund for Promotion of Scientific Research in Austria (FWF) under contract P08929-PHY.

1 Introduction

The violation of CP symmetry was first reported in 1964 by J.H. Christenson, J.W. Cronin, V. Fitch and R. Turlay, who detected a clean signal of $K_L \to \pi^+\pi^-$ decays [1]. CP conservation implies that the K_S and K_L particles are pure CP eigenstates and that K_L decays only into CP=-1 and K_S into CP=$+1$ final states. The observed signal of the forbidden $K_L \to 2\pi$ decays (CP=$+1$) indicates that CP is not a conserved symmetry.

CP violation can occur via the mixing of CP eigenstates, called *indirect* CP violation, represented by the parameter ε. CP violation can also occur in the decay process itself, through the interference of final states with different isospins. This is represented by the parameter ε' and is called *direct* CP violation. L. Wolfenstein in 1964 [2] proposed a super-weak force responsible for ΔS=2 transitions, so that all observed CP violation phenomena come from mixing and ε'=0. In 1973, Kobayashi and Maskawa proposed a matrix representation of the coupling between fermion families [3]. In the case of three fermion generations, both direct and indirect CP violation are naturally accommodated in their model, via an irreducible phase.

The parameters ε and ε' are related to the amplitude ratios

$$\eta_{+-} = \frac{\mathrm{A}(K_L \to \pi^+\pi^-)}{\mathrm{A}(K_S \to \pi^+\pi^-)} = \varepsilon + \varepsilon'$$

and

$$\eta_{00} = \frac{\mathrm{A}(K_L \to \pi^0\pi^0)}{\mathrm{A}(K_S \to \pi^0\pi^0)} = \varepsilon - 2\varepsilon'$$

which represent the strength of the CP violating amplitude with respect to the CP conserving one, in each mode. Experimentally, it is convenient to measure the double ratio R which is related to the ratio ε'/ε:

$$R = \frac{\Gamma(K_L \to \pi^0\pi^0)}{\Gamma(K_S \to \pi^0\pi^0)} \Big/ \frac{\Gamma(K_L \to \pi^+\pi^-)}{\Gamma(K_S \to \pi^+\pi^-)} \approx 1 - 6 \times \mathrm{Re}(\varepsilon'/\varepsilon) \qquad (1)$$

By the mid-1970s, experiments had demonstrated that CP violation in the neutral kaon system is dominated by mixing, with the limit $\mathrm{Re}(\varepsilon'/\varepsilon) \leq 10^{-2}$[4]. On the other hand, theoretical work showed that direct CP violation in the Standard Model could be large enough to be measurable [5]. This stimulated experimental effort with sophisticated detectors to measure $\mathrm{Re}(\varepsilon'/\varepsilon)$. The first evidence for the existence of a direct component of CP violation was published in 1988 [6]. In 1993, two experiments published their final results without a conclusive answer on the existence of this component. NA31 [7] measured $\mathrm{Re}(\varepsilon'/\varepsilon) = (23.0 \pm 6.5)\times10^{-4}$, indicating a 3.5σ effect. The result of E731 [8], $\mathrm{Re}(\varepsilon'/\varepsilon) = (7.4 \pm 5.9)\times10^{-4}$, was compatible with no effect. Recently, a new more precise generation of experiments announced results from samples of their total statistics. The KTeV collaboration measured an effect of $\mathrm{Re}(\varepsilon'/\varepsilon) = (28.0 \pm 4.1)\times10^{-4}$ [9] and NA48 published a first result of $\mathrm{Re}(\varepsilon'/\varepsilon)=(18.5 \pm 7.3)\times10^{-4}$ [10]. These observations confirmed the existence of a direct CP violation component. Current theoretical predictions are in the range up to $\sim30\times10^{-4}$ [11].

This paper reports a measurement of $\mathrm{Re}(\varepsilon'/\varepsilon)$ with increased precision, performed by the NA48 experiment, using data samples recorded in 1998 and 1999. The corresponding statistics is seven times larger than that used for the published 1997 result [10].

2 The method

Measuring $\mathrm{Re}(\varepsilon'/\varepsilon)$ to a precision of $\sim 10^{-4}$ requires several million K_L and $K_S \to \pi\pi$ decays. A sufficiently large flux of kaons is produced by the high intensity proton beam from the SPS accelerator. Data are accumulated using a fast and efficient data acquisition system, including a trigger with high rejection power and a large capacity data storage system.

The design of the experiment and the analysis method focus on making the inevitable systematic biases in the event counting symmetric between at least two of the four components of the double ratio. In this way, most of the important systematic effects cancel to first order, and only the differences between two components need to be considered in detail in the analysis. This allows the systematic uncertainties to be kept sufficiently low.

In order to exploit the cancellations, all four modes are collected at the same time and from the same decay volume. To achieve this, simultaneous K_S and K_L beams are produced in two targets situated at different distances from the decay volume. The intensity ratio is such that the $\pi\pi$ decay rates from the two beams are comparable. The kaon production angles are tuned to minimise the difference in the $K_L \to \pi\pi$ and $K_S \to \pi\pi$ decay spectra over a large range of kaon energies. The beam axes are almost collinear, both pointing to the centre of the detector, so that the decay products illuminate the detector in a similar way. The similarity is further enhanced by weighting each K_L decay by a function of its proper time, such that the K_L decay distribution becomes almost identical to that of K_S. The small remaining differences in beam divergences and beam geometries are corrected using Monte Carlo simulation. The small difference between K_S and K_L slow beam intensity variations are eliminated by weighting the K_S events by the K_L/K_S intensity ratio.

As a consequence of simultaneous data collection all losses associated with the detector, trigger and reconstruction efficiencies, and with the beam activity, cancel to a large extent between K_L and K_S. The ratio of $\pi^0\pi^0$ and $\pi^+\pi^-$ decays in each beam is independent of the absolute flux.

K_S decays are distinguished from K_L decays by means of tagging. Protons directed to the K_S target pass through a high-rate tagging station (see section 4.1). K_S events can be identified by comparing the registered proton time to the event time. Since this method is used for both the $\pi^0\pi^0$ and the $\pi^+\pi^-$ samples, the double ratio depends only on the difference in the K_S misidentification probabilities between the two decay modes, and not on their absolute values.

Backgrounds affect differently each of the four modes in the double ratio. High resolution detectors are employed to achieve an efficient background rejection. Small remaining impurities due to three body K_L decays are carefully subtracted.

After applying selection criteria, the four $K \to \pi\pi$ decay modes are counted in a common 70 to 170 GeV kaon energy interval. In this interval, the K_S and K_L decay spectra are similar to within $\pm 15\%$ (Fig. 24). In order to reduce the influence of the residual spectrum differences on the result, the events are separated into twenty bins of kaon energy, each 5 GeV wide. The event counts in both the $\pi^+\pi^-$ and $\pi^0\pi^0$ modes are corrected for the $\sim 10\%$ probability of misassigning a K_L decay to the K_S beam due to the high proton rate in the tagging station. After applying all corrections bin by bin, the result is obtained by averaging the twenty double ratios. Remaining uncertainties from the reconstruction, mainly due to uncertainties in the detector calibration and the geometry, are evaluated using several independent methods.

3 Beams

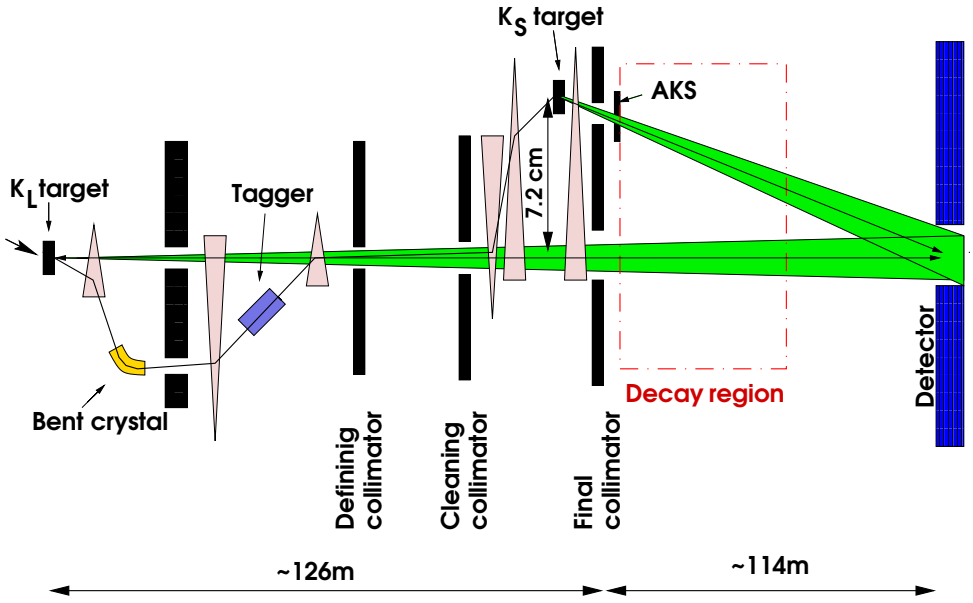

Figure 1: A schematic view of the beam line (not to scale).

The NA48 experiment is installed at CERN and uses the 450 GeV proton beam delivered by the SPS. K_L and K_S beams [12] are produced in different targets located 126 m and 6 m upstream of the decay fiducial region, respectively (Fig. 1).

The SPS has a cycle time of 14.4 s. It is filled with protons in two batches, each 11.5 μs long. The beam is accelerated to a momentum of 450 GeV/c with a 200 MHz radio-frequency system. It is then allowed to debunch, and is extracted by means of a slow excitation with 69 μs periodicity (3 SPS revolutions) over a spill length of 2.38 s. The small remnants of the typical frequencies (200 MHz, 100 MHz, 87 kHz and harmonics of 50 Hz) surviving the filtering and debunching, together with burst-to-burst fluctuations of the extraction, result in an effective spill length of $\sim$1.7 s. Since the K_S and K_L beams are produced concurrently, the K_S/K_L ratio is maintained stable throughout the burst to within $\pm$10%. This ensures that both beams are nearly equal in their sensitivity to intensity variations of the proton beam.

3.1 The K_L beam

The primary high-flux proton beam ($\sim 1.5\times10^{12}$ protons per pulse) impinges on a target (a 400 mm long, 2 mm diameter rod of beryllium), with an incidence angle of 2.4 mrad relative to the K_L beam axis. The charged component of the outgoing particles is swept away by bending magnets. The neutral beam passes through three stages of collimation. The first "defining" collimator, placed 41 m after the target, limits the opening angle of the beam. It is followed, 63 m further downstream, by a second "cleaning" collimator, which prevents particles scattered or produced on the aperture of the defining collimator from reaching the detectors. The fiducial region starts at the exit of the "final" collimator, 126 m downstream of the target. At this point, the neutral beam is dominated by long-lived kaons, neutrons and photons. Only a small fraction of the most energetic of the short-lived component (K_S and Λ) survives.

3.2 The K_S beam

The non-interacting protons from the K_L target are directed onto a mechanically bent mono-crystal of silicon [13]. A small fraction of protons satisfy the conditions for channelling and are deflected following the crystalline planes. This component passes through a small aperture collimator incorporated in a beam dump, which absorbs the main, undeflected beam of protons. The fine-tuning of the beam focusing and of the crystal position and angle with respect to the incoming proton direction allows to select the flux of protons transmitted to be $\sim 3\times10^7$ per pulse. Use of the crystal enables a deflection of 9.6 mrad to be obtained in only 6 cm length, corresponding to a bending power of 14.4 Tm. It acts only on the protons and guarantees a sharp emittance for the selected beam, without cancelling the deflection of the upstream sweeping magnet on other charged particles.

After the beam dump-collimator, the transmitted protons pass through the tagging station (see section 4.1) which precisely registers their time of passage. They are then deflected back onto the K_L beam axis, transported through a series of quadrupoles and finally directed to the K_S target (same size as K_L) located 72 mm above the K_L beam axis. A combination of collimator and sweeping magnet defines a neutral beam at 4.2 mrad to the incoming protons. The decay spectrum of kaons at the exit of the collimator is similar to that in the K_L beam, with an average energy of 110 GeV (Fig. 24).

The fiducial region begins 6 m downstream of the K_S target, such that decays are dominated by short lived particles. At this point, the K_S and K_L beams emerge from the aperture of the final collimators into the common decay region. The whole K_S target and collimator system is aligned along an axis pointing to the centre of the detector 120 m away, such that the two beams intersect at this point with an angle of 0.6 mrad. The whole decay region is contained in a 90 m long evacuated tank with a residual pressure of $\sim 5\times10^{-5}$ mbar, terminated by a thin composite polyamide (Kevlar) window of $3\times10^{-3}X_0$ thickness.

3.3 Particle rates in the decay region

It is important to keep the neutral kaon beams as free as possible from the contamination of particles, such as muons and scattered neutrons and photons, produced in the target or along the beam line. The 2.4 mrad production angle is chosen to reduce the neutron flux per useful K_L decay. Muons are reduced by the use of the bent crystal and by a further order of magnitude by the subsequent sweeping magnets. Beam halo particles are suppressed by means of multiple collimation and veto counters. Only 2×10^5 muons cross the detector for $\sim10^6$ K_L decays per spill, while the high fluxes of neutrons ($\sim10^8$) and photons ($\sim10^9$) in the neutral beam remain inside the beam pipe such that they do not reach the main detector. Since the fiducial decay region is enclosed in an evacuated tank interactions with air are minimised.

4 Detectors

The detector is shown in Fig. 2 [14]. Seven annular counters (AKL) surround the fiducial region to record photons escaping the acceptance of the main detector. Charged particles from decays are measured by a magnetic spectrometer. This is followed by a scintillator hodoscope which contributes to the trigger decision and also gives the precise time of charged decays. A liquid Krypton calorimeter is used to trigger and reconstruct $\mathrm{K}\to 2\pi^0$ decays. It is also used, together with a subsequent iron-scintillator calorimeter to measure the total visible energy for triggering purposes. Finally, at the end of the beam

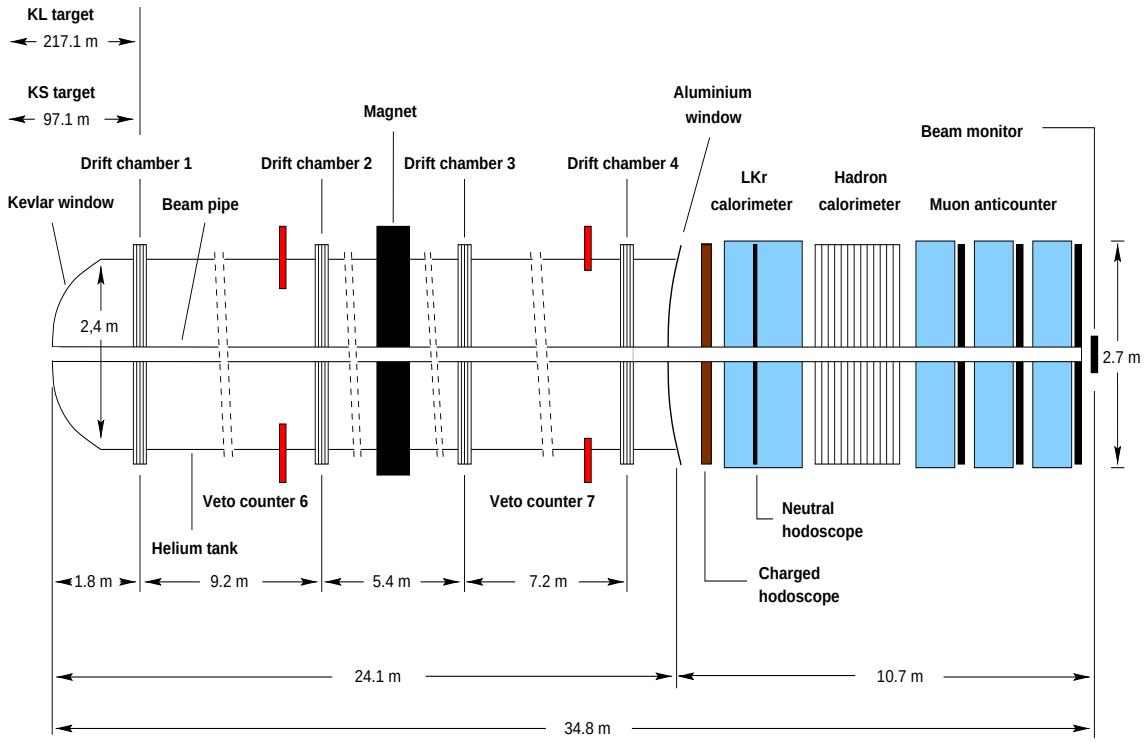

Figure 2: The detector.

line, a series of muon counters are used to identify $K_L \to \pi\mu\nu$ ($K_{\mu 3}$) decays.
Two beam counters are used to measure the intensity of the beams. One is located at the extreme end of the K_L beam line (K_L monitor) and the other (K_S monitor) is at the K_S target station.

4.1 The tagging station

The tagging station (or Tagger) is located on the K_S proton path after the bent crystal. It consists of two scintillator ladders, crossing the beam horizontally and vertically [15]. All scintillators are 4 mm thick in the beam direction and 15 mm long. To equalise the proton counting rate in all channels each ladder comprises 12 scintillators of variable widths, from 0.2 mm at the centre to 3.0 mm at the edges. An overlap of 50 μm between two successive counters ensures that the beam is completely covered. The scintillators of vertical and horizontal ladders alternate along the beam direction (Fig. 3). A proton crosses at least two of them, one horizontal and one vertical. Photomultiplier

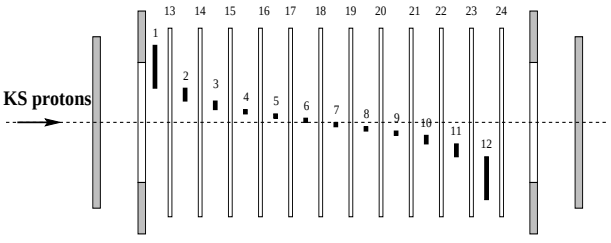

Figure 3: The arrangement of the counters of the tagging station. Counters 1-12 are oriented horizontally and counters 13-24 vertically.

pulses are digitised by an 8-bit 960 MHz flash ADC module [16]. A ∼100 ns window is

read out around the trigger time. The reconstructed time per counter has a resolution of ∼140 ps, and two close pulses can be resolved down to 4–5 ns. Proton times are reconstructed offline by combining the information from horizontal and vertical counters. The coincidence of this time with the event time assigns the decay to the K_S beam. A demonstration of the principle is given in Fig. 4 for $\pi^+\pi^-$ decays, where the difference of the event time from the closest proton time as a function of the vertex position in the vertical plane clearly shows the K_S and K_L beam assignment.

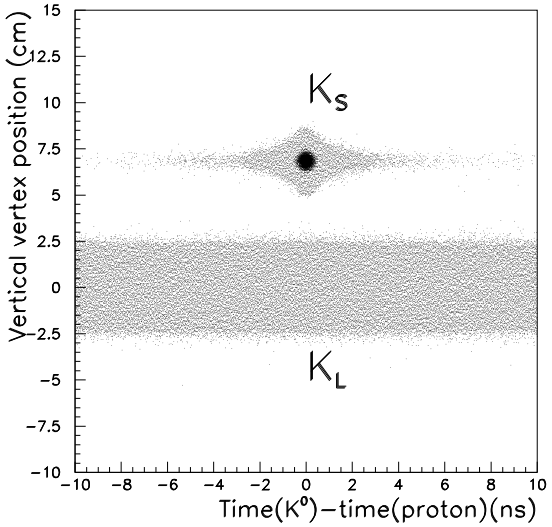

Figure 4: Time difference between event and its closest proton for $K_S, K_L \to \pi^+\pi^-$ events as a function of the vertical position of their decay vertex.

4.2 The magnetic spectrometer

The spectrometer is housed in a tank filled with helium gas at atmospheric pressure. A thin evacuated beam tube allows the neutral beam to continue in vacuum. Two drift chambers (DCH1 and DCH2) are located before, and two (DCH3 and DCH4) after, the central dipole magnet. These chambers and their interconnecting beam tube are aligned along the bisector between the converging K_S and K_L beam axes.

The integral of the magnetic field is 0.883 Tm, corresponding to an induced transverse momentum kick of 265 MeV/c in the horizontal plane. All components of the field have been measured. During the run, the current in the magnet is recorded and any relative variation larger than 5×10^{-4} is corrected for. The momentum scale is set adjusting the reconstructed invariant mass in $\pi^+\pi^-$ decays to the nominal K^0 mass.

The drift chambers have an octagonal shape and an area of 4.5 m^2 [17]. Each is made up of four sets of two staggered sense wires planes oriented along four directions, each one rotated by 45° with respect to the previous one, and all orthogonal to the beam. This permits charged tracks to be reconstructed without ambiguities, and minimises the effect of wire inefficiencies by providing redundant information. The wire material of the eight planes and the filling gas correspond to 0.4% X_0 per chamber. Only four planes of DCH3 are instrumented.

With such large chambers, it is important to know the linear dimensions accurately and to have good control of the uniformity. The geometric accuracy due to the cumulative

uncertainty on the wire positions is better than 0.1 mm/m. In addition, the average plane efficiency is measured to be greater than 99%, radially uniform to ± 0.2% (Fig. 5.a).

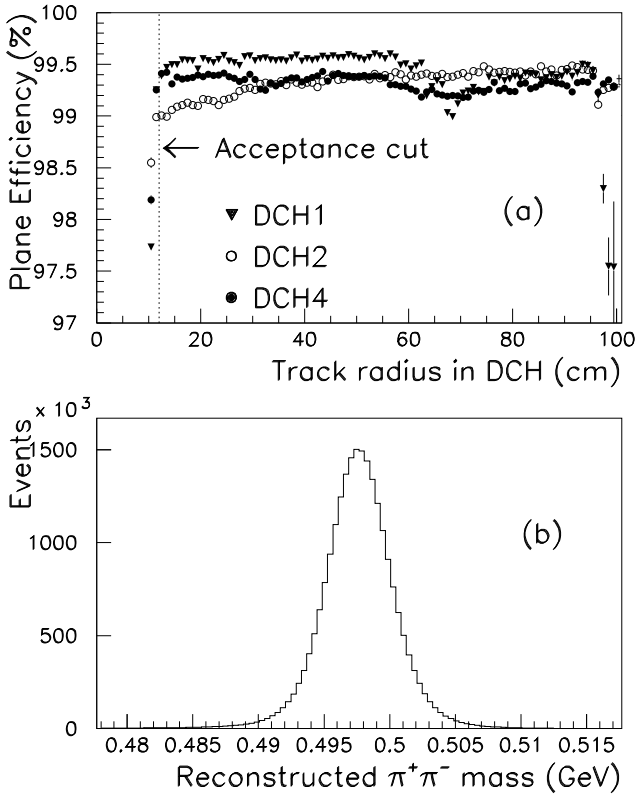

Figure 5: Plane efficiencies for DCH1,DCH2 and DCH4 as a function of the track radius (a). Reconstructed $\pi^+\pi^-$mass (b).

A short drift distance (5 mm, corresponding to a drift time of 100 ns) contributes to the high rate capability of this detector. Track positions are reconstructed with a precision of 100 μm per view. The momentum resolution, obtained from the analysis of special electron runs, is $\sigma(p)/p = 0.48\% \oplus 0.009 \times p\%$, where p is in GeV/c. The resolution of the invariant $\pi^+\pi^-$ mass is 2.5 MeV/c^2 (Fig. 5.b). The track reconstruction provides an event time with a precision of 0.7 ns. This is used to cross-check the main charged event time determined by the scintillator hodoscope.

4.3 The scintillator hodoscope

A scintillator hodoscope is placed downstream of the helium tank. It is composed of two planes segmented in horizontal and vertical strips and arranged in four quadrants. Fast logic combines the quadrant signals, which are used in the first level of the trigger for charged events. Offline, a combination of hits located at the extrapolated $\pi^+\pi^-$ track positions is used to reconstruct the charged event time with a precision of ∼150 ps.

4.4 The liquid Krypton calorimeter

The liquid Krypton calorimeter (LKr) is a quasi-homogeneous detector with an active volume of ∼10 m^3 of liquid Krypton. Cu-Be-Co ribbons of 40 μm × 18 mm × 125 cm define ∼13000 cells, in a structure of longitudinal projective towers pointing to the centre of the decay region [18]. The calorimeter is 27 X_0 long and fully contains

electro-magnetic showers with energies up to 100 GeV. The cross section of a cell is about 2 cm × 2 cm, and consists of a central anode in between two cathodes. The electrodes are guided longitudinally through precisely machined holes in five spacer plates located every 21 cm. They follow a ±48 mrad zig-zag in order to maintain the mechanical stability and to decrease the sensitivity of the energy resolution to the impact position. Good energy response is further guaranteed by the initial current readout technique which also provides a high rate capability. The signals are shaped to ∼75 ns FWHM and are digitised asynchronously by a 40 MHz flash ADC [19]. The dynamic range of the digitisers is increased by gain-switching amplifiers which change the amplification factor depending on the pulse height. The calorimetric information readout is restricted by a zero-suppressing hard-wired programmable algorithm to channels belonging to an energy dependent halo around the most energetic impact cells. The calorimeter was operated in a stable way at a high voltage of 3 kV. Around 0.3% of the cells were defective and are excluded from the analysis.

The performance of the calorimeter [20] is studied using the electrons from the abundant $K_L \to \pi e\nu$ (K_{e3}) sample recorded along with the $\mathrm{Re}(\varepsilon'/\varepsilon)$ data taking. The electrons are used to improve the cell-to-cell uniformity from 0.4% after electronic calibration to 0.15%. To avoid possible correlations between non-linearity and non-uniformity, only electrons in the energy range 25–40 GeV were used for this purpose. Cell-to-cell calibration factors were checked using photons from π^0 and η decays in special runs.

Fig. 6 shows the resolution of the ratio E/p of energy (from the LKr) and momentum (from the spectrometer), obtained using K_{e3} events after the inter-calibration procedure. Unfolding the measured contribution of the spectrometer to the momentum resolution, the following energy resolution is obtained, with E in GeV:

$$\frac{\sigma(E)}{E} = \frac{(3.2 \pm 0.2)\%}{\sqrt{E}} \oplus \frac{(9 \pm 1)\%}{E} \oplus (0.42 \pm 0.05)\%$$

The $3.2\%/\sqrt{E}$ sampling term is dominated by the fluctuations of the shower fraction outside the cluster radius used in the reconstruction. The 1/E term is given by the total noise in the cluster. The constant term has contributions from the cell-to-cell calibration, the residual gap width variations, the response variation with impact distance from the electrodes and the pulse reconstruction accuracy.

The energy response is linear to about 0.1% in the range 5–100 GeV. This is shown in Fig. 7, where the average E/p is shown for electrons. To account for losses in the material in front of the calorimeter, 45 MeV is added to the electron energy as computed by a GEANT-based Monte Carlo [26]. This simulation also predicts a 0.05% non-linearity because of the slight change in the electrode gap width, due to the projective geometry of the calorimeter. This effect is only significant for high energy showers which develop deeper inside the calorimeter.

The position resolution of the calorimeter is measured using monochromatic electron beams. Comparing the electron centre of gravity position from the nine cells around the impact point with the extrapolated track point, one finds a resolution better than 1 mm in both directions, for energies above 25 GeV (the average of the photon spectrum).

The calorimeter gives an accurate time signal for neutral events, which is then used together with the tagging station time measurements to distinguish K_S from K_L. The photon time resolution is of the order of 500 ps in the energy range from 3 to 100 GeV. The $2\pi^0$ event time is known with a precision of ∼220 ps. Tails coming from

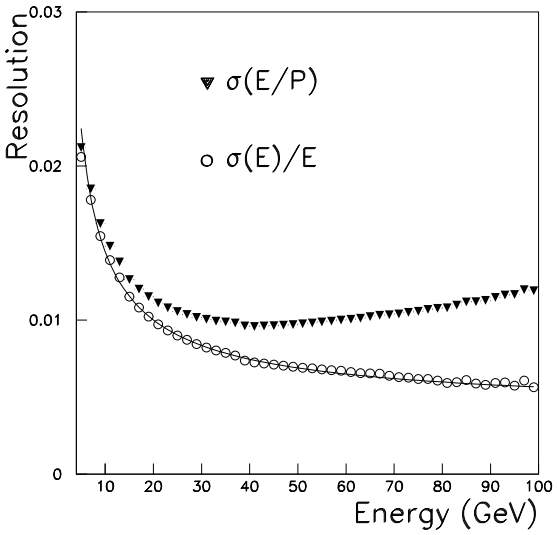

Figure 6: Energy resolution of the LKr calorimeter, obtained with electrons from $K_L \to \pi e \nu$ decays.

misreconstructed times have been studied using a single K_S beam; they are below the level of 10^{-4}.

4.5 The K_S anti-counter

The K_S anti-counter (AKS) is located at the exit of the K_S collimator. It is composed of a photon converter followed by three scintillator counters, and its main purpose is to veto all upstream decays from the short-lived beam. The converter consists of a 2.96 mm thick iridium crystal of 1.8 X_0 [21], which converts photons into electron pairs keeping the diffraction probability small. The crystal axis is aligned with the beam axis to maximise the pair production. Given the measured conversion efficiency, only 2.1×10^{-4} of the accepted $K_S \to 2\pi^0$ sample are due to decays occuring upstream of the AKS.

Charged particles, whether from photon conversion in the crystal or from $\pi^+\pi^-$ decays, are detected by the scintillator counters. The time is reconstructed offline with a resolution of about 160 ps. The inefficiency of the measurement is due to the intrinsic counter inefficiency and the dead-time of the subsequent readout system, which might affect the detection of $K_S \to \pi^+\pi^-$. This results in a total inefficiency of 1.0×10^{-4}. The final double ratio is therefore corrected by $(1.1\pm0.4)\times10^{-4}$ for the difference in the AKS inefficiency between $\pi^0\pi^0$ and $\pi^+\pi^-$ modes.

The AKS counter is used offline to define the beginning of the decay region for the K_S beam. An event is rejected if a hit is recorded in time by the second scintillator. The AKS counter plays therefore an essential role in the experiment: the iridium crystal and the second scintillator give the geometrical references needed to control the energy scale and to define the fiducial region for K_S decays into $\pi^0\pi^0$ and $\pi^+\pi^-$ respectively.

4.6 Hadron calorimeter and muon counters

A calorimeter made of iron and scintillators, 6.7 nuclear interaction lengths thick, measures hadronic energy. It contributes, together with the LKr calorimeter, to the total energy trigger. Following the hadron calorimeter are the muon counters. Three planes of scintillators shielded by 80 cm thick iron walls provide timing information that is used

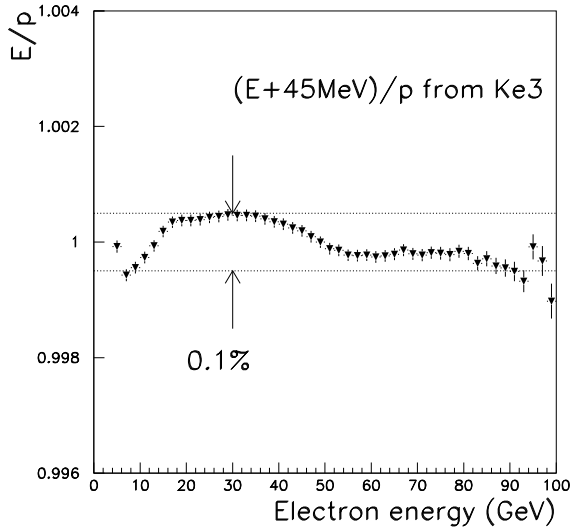

Figure 7: The linearity of the LKr calorimeter, obtained with electrons from $K_L \to \pi e \nu$ decays.

offline to identify the background from $K_L \to \pi \mu \nu$ ($K_{\mu 3}$) decays.

5 Triggers and data acquisition

The rate of particles reaching the detector is around 500 kHz. The trigger is designed to reduce this rate, with minimal loss from dead time and inefficiencies, to several kHz. A part of the read-out rate is reserved for redundant low-bias triggers that collect data used for the direct determination of the trigger inefficiencies.

The trigger decisions are collected in a trigger supervisor system [22] that records the time of the accepted events, relative to the 40 MHz clock signal used to synchronise the experiment over its entire 250 m length [23]. The combined trigger decision is sent back to all the read-out elements in the form of a time stamp. This time stamp arrives no later than 200 μs after the event occurrence, while all data are buffered in the front-end electronics. The time stamp is transformed into an address location in the buffer. A sufficiently large time interval (100–250 ns depending on the subdetector) around this location is read out and written to tape. In case of an occasional pile-up of positive trigger decisions, consecutive time stamps are queued to allow all subsystems to send their data to the event builder before receiving another time stamp. If, nevertheless, one of the subsystems fails to send the complete data, the whole trigger system is blocked, ensuring equal losses for $\pi^+\pi^-$ and $\pi^0\pi^0$ decays. Event building is performed in an on-site PC farm and transmitted via a Gigabit network to the CERN computer centre, where another PC farm controls the tape writing and carries out the data reconstruction and the monitoring of the experiment.

5.1 Trigger for $\pi^0\pi^0$ decays

The trigger for $\pi^0\pi^0$ decays [24] operates on the analogue sums of signals from 2×8 cells of the LKr calorimeter, in both horizontal and vertical orientations. The signals are digitised, filtered to reduce noise and summed into 64 columns and 64 rows, thus providing two projections of the energy deposited. The summed energy E is computed along with the first and second moments of the energy distribution in each projection, $M_{1,x}$, $M_{1,y}$, $M_{2,x}$ and $M_{2,y}$. The moments are converted into kinematic quantities using a

"look-up table" system. The radial position of the centre of gravity, $C = \sqrt{M_{1,x}^2 + M_{1,y}^2}/E$, is an estimate of the distance between the kaon impact point at the calorimeter plane (had it not decayed) and the beam axis. The distance of the decay vertex from the calorimeter, $D = E\sqrt{(M_{2,x} + M_{2,y})/E - C^2}/m_K$, where m_K is the kaon mass, is computed to determine the proper time of the kaon decay. In addition, the number of energy peaks, in space and in time, in both vertical and horizontal projections, is computed in bins of 3 ns.

The trigger requires an electro-magnetic energy deposit greater than 50 GeV, along with $C < 15$ cm and a decay vertex less than 5 K_S lifetimes (τ_S) from the beginning of the decay volume. Another requirement, that there are less than 6 peaks within 9 ns in both projections, helps to reject background from $K_L \to 3\pi^0$. This condition is released, however, if accidental activity is detected close in time.

The electronics is implemented in a pipeline which makes the trigger free of dead time. The resulting rate of this trigger component is 2 kHz with a latency of 3 μs.

The efficiency is measured with events triggered by a scintillating fibre hodoscope placed at the depth of about 9.5 X_0 near the shower maximum in the LKr calorimeter. It is (99.920±0.009)%, with no significant difference between K_S and K_L decays. Therefore no correction to the $\mathrm{Re}(\varepsilon'/\varepsilon)$ measurement is applied. The inefficiency is dominated by losses from an unresolved pile-up with accidental hits and by occasional energy mismeasurement. A cross-check of the efficiency measurement was performed with a very loose trigger condition ($E >$15 GeV) applied to events collected in single K_S-beam runs.

5.2 Trigger for $\pi^+\pi^-$ decays

The $\pi^+\pi^-$ decays are triggered with a two-level trigger system. At the first level, the rate is reduced to 100 kHz by a coincidence of three fast signals:

1. Opposite quadrant coincidence in the scintillator hodoscope (Q_x), where the quadrants are defined with some overlap in order to avoid geometric inefficiencies. The remaining inefficiency (0.05%) is due to electronics and scintillator geometry, and is equal for K_S and K_L decays. However, a Q_x signal cannot be produced in two consecutive 25 ns clock periods, which leads to a dead time of 0.5%. Signals in a sufficiently large time window are recorded to allow the dead time to be applied (offline) on an event-by-event basis also to the $\pi^0\pi^0$ sample.
2. Hit multiplicity in DCH1 integrated over 200 ns, requiring at least 3 wires hit in at least 3 views ($2track$). This has an inefficiency smaller than 10^{-4}.
3. Total calorimetric energy (E_{tot}), made by summing the electro-magnetic energy from the $\pi^0\pi^0$ trigger with the hadron calorimeter energy, is required to be more than 35 GeV. Owing to the low resolution in the time and size of the hadronic energy measurement, some good events fail to pass the energy threshold or the time coincidence with the Q_x and $2track$ signals. The E_{tot} efficiency is $(99.542 \pm 0.018)\%$ for K_L events (proper-time weighted) and $(99.535 \pm 0.011)\%$ for K_S events. The correction for the efficiency difference is applied in bins of energy and amounts to $(0.9 \pm 2.2)\times10^{-4}$ on the average double ratio.

A signal composed of $Q_x \times 2track \times E_{tot} + Q_x/D$ is sent to the second level trigger with a latency of 5 μs. The Q_x/D component, where D denotes a down-scaling factor, is added in order to measure the efficiencies of the $2track$ and E_{tot} components. An additional down-scaled $2track \times E_{tot}$ trigger signal by-passes the second level trigger to allow efficiency measurements of the Q_x signal and of the second level trigger.

The second level of the $\pi^+\pi^-$ trigger [25] consists of hardware coordinate builders and a farm of asynchronous microprocessors that reconstruct tracks using data from DCH1, 2 and 4. Triggers are selected if the tracks converge to within 5 cm, their opening angle is smaller than 15 mrad, the reconstructed proper decay time is smaller than 4.5 τ_S, and the reconstructed $\pi\pi$ mass is larger than 0.95 m_K. The latency is variable but does not exceed 100 μs and the output rate is 2 kHz. The efficiency is (98.319±0.038)% for K_L (proper-time weighted) and (98.353±0.022)% for K_S decays. The inefficiencies are due mainly to DCH wire inefficiencies (1.2%) with a contribution from algorithm imprecision (0.3%) and misreconstructions from accidental hits (0.2%). The correction for the second level trigger efficiency difference is applied in bins of energy with an average of $(-4.5 \pm 4.7)\times10^{-4}$ on R.

The time available to extract the data from the spectrometer read-out ring buffers to the second level trigger is limited. This leads to a 1.1% dead time. The same dead time condition is applied to $\pi^0\pi^0$ candidates event by event, to ensure that the principle of collecting $\pi^+\pi^-$ and $\pi^0\pi^0$ decays concurrently is respected.

In order to avoid recording events with high hit multiplicity, an overflow condition is generated in the drift chamber readout whenever more than seven hits in a plane are detected within 100 ns. In this case the front end readout buffers of this plane are cleared and the time of the overflow is recorded. Both the second level trigger and the reconstruction of events are affected by this condition.

Overflows are mainly due to showers induced by interactions of electrons or photons in the material surrounding the beam pipe in the region of the spectrometer and by δ-rays coming from interactions of charged particles with the drift chamber gas. Occasionally they are also generated by noisy amplifiers operated with low thresholds. In this case at most two neighbouring planes are affected.

In the offline reconstruction, a window of ±312 ns around the event time is required to be free of overflows, both for $\pi^+\pi^-$ and $\pi^0\pi^0$ decays. This time window is larger than the sum of maximum drift time and reset time. In the $\pi^0\pi^0$ sample 21.5% of events are removed by the overflow condition which reduces the sensitivity to K_S/K_L intensity variations by an order of magnitude.

5.3 Other triggers

Several other triggers were collected continuously during data taking for systematic studies:

- A trigger for $3\pi^0$ decays, given by the down-scaled $\pi^0\pi^0$ trigger without the peak condition, used for K_S tagging studies.
- A trigger for $\pi^0\pi^0_D$ (where π^0_D stands for the Dalitz decay $\pi^0_D \to ee\gamma$) decays, combining the information from the LKr calorimeter and the spectrometer, used to test K_S tagging and the energy scale.
- Beam monitor triggers used to record the accidental activity, with rates proportional to K_L and K_S decay rates. Beam monitor signals are down-scaled and delayed by 69 μs which corresponds to the periodicity of the slow proton extraction (3 SPS revolutions).
- Calibration triggers used to monitor and calibrate the LKr calorimeter, the tagging station and the scintillator hodoscope.

6 Data samples

The NA48 experiment collected data for the $\mathrm{Re}(\varepsilon'/\varepsilon)$ measurement in SPS running periods during the summer of three consecutive years: 1997–1999. The data from the first running period yielded 0.49 million $K_L \to 2\pi^0$ events. The result was published in [10].

In the year 1998, the total number of $K_L \to 2\pi^0$ events collected during 135 days of running was 1.1 million. In the year 1999, an upgrade of the trigger and the event builder PC farm, as well as an increase in the operational stability of the detectors and electronics, contributed to obtaining smaller dead time and higher data taking efficiency. In addition, the SPS spill length was increased by 10%. This allowed the experiment to collect 2.2 million $K_L \to 2\pi^0$ events in 128 days. In all run periods the polarity of the magnetic field was regularly inverted to allow systematic checks on $\pi^+\pi^-$ decay reconstruction.

In the year 2000, a special run took place to cross-check the K_S tagging systematics. In this run, the NA48 detector operated with vacuum in place of the spectrometer, and with the K_S-protons swept away after their passage through the tagging station. This allowed a direct measurement of the accidental coincidence rate between the $K_L \to 2\pi^0$, $3\pi^0$ decays and the protons passing through the Tagger.

Along with simultaneous K_L and K_S beam runs, several auxiliary runs were dedicated to various systematic checks. Data with muon or with K_L beams without the spectrometer magnetic field were taken for alignment purposes. Scans with a monochromatic collimated electron beam were used for spectrometer and calorimeter calibration and alignment. Runs with either K_S or K_L beam only were taken on a regular basis to verify the K_S tagging performance and to check the data quality in single beam conditions. Tests of the LKr calorimeter calibration were carried out using data from runs with two thin polyethylene targets exposed to a π^- beam producing $\pi^0 \to \gamma\gamma$, $\eta \to \gamma\gamma$ and $\eta \to 3\pi^0$ decays at precisely defined vertex positions.

7 Decay identification

The raw data amount to 170 TBytes. After decoding and hit reconstruction, the data were filtered and compacted in several steps to allow for the iterative improvement of calibrations, alignment and corrections. The last step, before the final event selection, was sufficiently fast that it could be repeated several times following the refinements of the corrections.

7.1 Reconstruction and selection of $\pi^0\pi^0$ events

The reconstruction of $\pi^0\pi^0$ events is based entirely on data from the LKr calorimeter. The time and height of the pulses are measured using a digital filter technique. The first calibration is performed using a calibration pulser system. The cell response is inter-calibrated comparing energy and momentum (E/p) of electrons from K_{e3} data. Further checks and fine tuning of the inter-calibration by $\sim$0.1% were performed with π^0s produced in a π^- beam by adjusting the reconstructed vertex of the photon pairs to the target position.

Small drifts of the pedestal due to temperature effects are monitored and corrected. A pile up of signals within 3 μs causes the pedestal to shift. These shifts are detected by comparing ADC samples, stored in a buffer before the trigger, with the average pedestal level. If there is a significant difference between the two, then the stored samples are used; otherwise, the average pedestal is taken. This procedure minimises the influence of noise on the pulse height measurement.

Photon showers are found by looking for maxima in the digitised pulses from individual cells in both space and time, and accumulating the energy within a radius of 11 cm. The shower position is derived from the centre of gravity of 3×3 central cells. Both energy and position measurements are corrected for a dependence on the distance of the impact point to the electrodes using data from electron beam scans. The transverse scale of the calorimeter is checked using K_{e3}-electron tracks and residuals of $\sim$200 μm are applied as a correction to cluster positions. In order to account for deviations from the projectivity of the calorimeter, the cluster positions are recomputed at the shower maximum depth. The expected shower depth is estimated from K_{e3} data comparing reconstructed and extrapolated electron shower positions and extrapolated to photons using Monte Carlo simulations.

Overlapping showers are separated using expected shower shapes from a GEANT Monte Carlo simulation. The quality of the shower shapes is tested with data from electron beam scans. Based on these data, an additional correction is applied at the reconstructed shower level. Energy losses at the borders of the calorimeter are also accounted for, using information from Monte Carlo simulations and electron beam scans. Zero-suppression bias in showers with energy smaller than 5 GeV is reduced by parametrising the ratio of the energies deposited in a well defined 7×7 cell shower box and the total reconstructed shower energy, as a function of the photon energy and the number of cells read out. A small decrease of measured energy due to space charge accumulation during the spill, in average around 1.5×10^{-4}, is corrected using K_{e3} data [27]. The average energy loss of photons in the material before the calorimeter was determined with GEANT Monte Carlo to be 15 MeV. Shower energies are increased by this amount. A correction for residual nonlinearity of the energy measurement is derived from the parametrised E/p distribution of K_{e3}-electrons (Fig. 7).

Correct shower reconstruction is ensured by accepting only showers with energies between 3 and 100 GeV, and positions more than 15 cm from the calorimeter centre, 11 cm from its outside borders and 2 cm from any defective cell.

Any group of four showers, each reconstructed within 5 ns of their average time, is examined for the $\pi^0\pi^0$ signature. A minimum distance of 10 cm between the showers is required to resolve correctly the overlapping energy deposits. The event time is computed from an energy-weighted average of time measurements in individual cells, using the two cells with the largest energy deposits in each shower. Cells with signals more than 5 ns from the average time are excluded from the time computation.

The distance d_{vertex} of the decay vertex from the LKr calorimeter is computed from the energies E_i and positions (x_i, y_i) of the four showers, with the assumption that they come from the decay of a particle with the kaon mass m_K moving along the beam axis:

$$d_{vertex} = \frac{\sqrt{\sum_{i}^{4} \sum_{j>i}^{4} E_i E_j \left((x_i - x_j)^2 + (y_i - y_j)^2\right)}}{m_K} \tag{2}$$

A resolution of $\sim$50 cm is obtained on d_{vertex}. The vertex position z_{vertex} is equal to $z_{LKr} - d_{vertex}$. The invariant mass of two photons $m_{\gamma\gamma}$ is then computed as

$$m_{\gamma\gamma} = \frac{\sqrt{E_1 E_2 \left((x_1 - x_2)^2 + (y_1 - y_2)^2\right)}}{d_{vertex}} \tag{3}$$

The two $m_{\gamma\gamma}$ masses (m_1 and m_2) are anti-correlated (Fig. 8) because d_{vertex} contains information from all four showers. In order to find the best shower pairing, a χ^2 variable

is constructed. In this variable, m_1 and m_2 values are combined in order to remove the anti-correlation.

$$\chi^2 = \left[\frac{\frac{(m_1+m_2)}{2} - m_{\pi^0}}{\sigma_+}\right]^2 + \left[\frac{\frac{(m_1-m_2)}{2}}{\sigma_-}\right]^2 \tag{4}$$

where σ_+ and σ_- are the corresponding resolutions, parametrised as functions of the energy of the least-energetic photon. The average values of σ_+ and σ_- are 0.42 MeV/c^2 and 0.83 MeV/c^2, respectively.

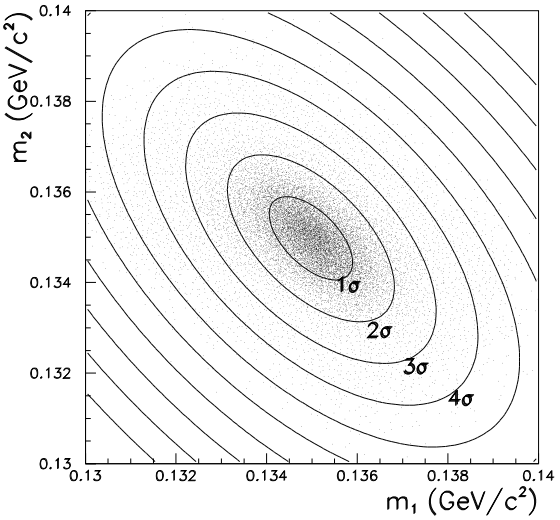

Figure 8: Distribution of $K_S \to 2\pi^0$ candidates in the space of two reconstructed $m_{\gamma\gamma}$ masses, m_1 and m_2. The contours correspond to increments by one standard deviation.

As electrons and photons have different energy losses, the final adjustment of the energy scale is done with photons. The energy scale is directly coupled to the distance scale (Eq. 2). It is adjusted by comparing the average vertex position of $K_S \to 2\pi^0$ candidates at the AKS edge with that produced by the Monte Carlo (Fig. 9), with an accuracy of 3 cm. The adjustment of the energy scale is applied as a function of the run period.

The sensitivity of the double ratio to the energy scale is minimised by the choice of both the kaon energy range and the fiducial decay volume. At the chosen energy boundaries, 70 to 170 GeV, the shape of the decay spectrum favours a cancellation of the losses and gains in case of an energy scale shift.

The total number of selected K_L decays is nearly independent of the distance scale because the acceptance is only weakly dependent on the longitudinal vertex position. For K_S decays the beginning of the decay volume is defined by the AKS counter. The end of the decay volume is chosen to be $3.5\tau_S$ downstream of the AKS. A 3 cm shift in this cut, corresponding to the accuracy of the energy scale adjustment, together with the effects of energy boundaries and acceptance, would lead to an error of 2×10^{-4} in the decay rates.

All systematic uncertainties in the $\pi^0\pi^0$ reconstruction are summarised in Tab. 1. The residual deviation from linearity in the photon energy measurement was parametrised as:

$$\Delta E = \alpha + \beta E^2 + \gamma r E \tag{5}$$

where E is the energy of the photon shower, and r is its distance from the centre of the calorimeter. An upper limit for each of the coefficients α, β, γ is determined on the basis

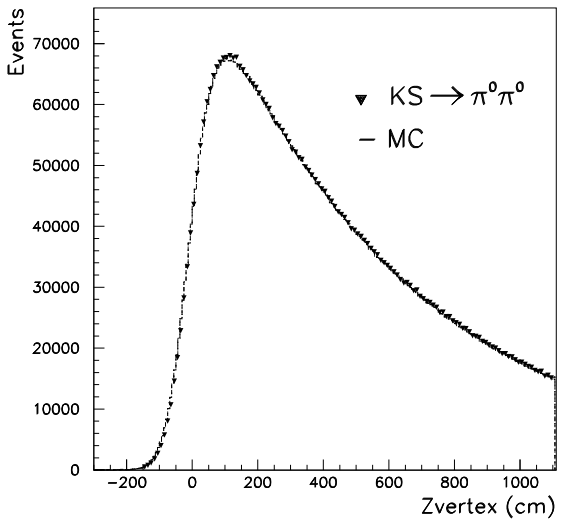

Figure 9: Distribution of the reconstructed vertex position z_{vertex} of the $K_S \to \pi^0\pi^0$ candidates at the beginning of the decay volume. The origin of the z_{vertex} axis is set to the nominal AKS position.

of the observed nonlinearities in K_{e3} decays (Fig. 7), in $K \to 2\pi^0$, $3\pi^0$ decays, and π^0 and $\eta \to \gamma\gamma$ decays from π^- beams. In addition, the stability of the energy scale is verified as a function of kaon energy (Fig. 10). The sensitivity of R to non-linearities is determined by modifying the reconstructed energies in the Monte Carlo. The modification takes into account also a non-linearity at $E_\gamma < 6$ GeV observed in $\pi^0 \to \gamma\gamma$ decays, not covered in the above parametrisation.

The values of the shower depth used for the position adjustment are checked by comparing electrons from K_{e3} with Monte Carlo simulations. The agreement is better than 2 cm, which corresponds to a systematic effect of 1.2×10^{-4}. The precision in the sharing of energies in overlapping showers is accounted for with a $\pm2.0\times10^{-4}$ uncertainty on R which is the size of the correction from the electron beam scan. The transverse scale of the LKr calorimeter, relative to the spectrometer, was verified with K_{e3}-electron tracks. The uncertainty on the double ratio of $\pm2.5\times10^{-4}$ corresponds to the difference between these data and measurement during the calorimeter construction corrected for the termal contraction.

Due to hadron photoproduction in the liquid krypton, significant asymmetric non-Gaussian tails arise in the measurement of energies in about 3×10^{-3} of photons. These tails are parametrised using electrons and π^0 decays and inserted into the Monte Carlo. The uncertainty associated to the effect of non-Gaussian tails is $\pm1.2\times10^{-4}$ on the double ratio.

The scale adjustment is verified by studying π^0 and η decays from a known origin produced by the π^- beam. Both the $\pi^0 \to \gamma\gamma$ and the $\eta \to \gamma\gamma$ samples give consistent results. For the latter, the η mass is determined from $\eta \to 3\pi^0$ decays, cross-checking the method with $K_L \to 3\pi^0$ decays[1)]. The linearity of the distance scale along the beam axis is checked by comparing the results with the two polyethylene targets placed 1462 cm apart. The distance measured from data agrees within 1 cm with the nominal value. This is consistent with the uncertainties on the radial non-linearity γ, shower maximum

[1)] To be published

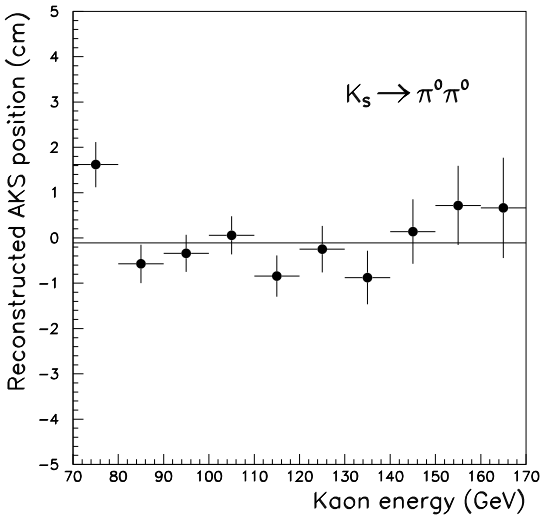

Figure 10: Reconstructed AKS position as a function of kaon energy for $K_S \to 2\pi^0$ events.

position and energy sharing from Tab. 1. Another check is performed with $K \to \pi^0\pi^0$ decays, with subsequent $\pi^0 \to ee\gamma$ decay, comparing the vertex reconstructed from the e^+e^- tracks to the one derived from the electro-magnetic showers.

7.2 Reconstruction and selection of $\pi^+\pi^-$ events

The $\pi^+\pi^-$ events are reconstructed from tracks using hits in the drift chambers of the spectrometer. First, clusters of hits in each pair of staggered planes are found. The pattern recognition is based on hit positions without using the drift times. Clusters in DCH1 and DCH2, within a range of 10–110 cm from the centre of the chamber, are assembled into track segments separately in each coordinate view (x, y, u, v). The segments are associated with space points in DCH4 with the constraint that the track is compatible with a straight line in the y view (vertical direction).

Each track candidate is converted into one or more tracks using the drift time information. Drift times are corrected for wire lengths and offsets using constants extracted from alignment runs with μ and K_L beams without the magnetic field. Among tracks

Table 1: Summary of systematic uncertainties on R in the $\pi^0\pi^0$ reconstruction.

	Units of 10^{-4}
Energy scale	± 2.0
Nonlinearity:	
$\quad \lvert\alpha\rvert < 1 \times 10^{-2}$ GeV	± 2.5
$\quad \lvert\beta\rvert < 2 \times 10^{-5}$ GeV^{-1}	± 2.3
$\quad \lvert\gamma\rvert < 1 \times 10^{-5}$ cm^{-1}	± 1.5
$\quad$ at $E_\gamma < 6$ GeV	± 1.5
Shower maximum	± 1.2
Energy sharing	± 2.0
Transverse scale	± 2.5
Non-Gaussian tails	± 1.2
Total	± 5.8

sharing the same space point in DCH4, the one with the best χ^2 is chosen. After adding DCH3 information, the track momenta are calculated using a measured magnetic field map and alignment constants.

A vertex position is calculated for each pair of tracks with opposite charge after correcting for a small residual magnetic field due to the magnetisation of the vacuum tank ($\sim 2{\times}10^{-3}$ Tm). The longitudinal vertex position resolution is about 50 cm, whereas the transverse resolution is around 2 mm. Only tracks with momenta greater than 10 GeV and not closer than 12 cm to the centre of each DCH are accepted. The separation of the two tracks at their closest approach is required to be less than 3 cm. The track positions, extrapolated downstream, are required to be within the acceptance of the LKr calorimeter and of the muon veto system, in order to allow for proper electron and muon identification.

The time of the $\pi^+\pi^-$ decay is determined from hits in the scintillator hodoscope associated with the tracks. The events with insufficient information to determine the decay time accurately are discarded. This inefficiency is 0.1% and is equal for K_S and K_L.

The kaon energy is computed from the opening angle θ of the two tracks before the magnet and from the ratio of their momenta p_1 and p_2 assuming a $K \to \pi^+\pi^-$ decay:

$$E_K = \sqrt{\frac{\mathcal{A}}{\theta^2}(m_K^2 - \mathcal{A}m_\pi^2)} \tag{6}$$

where

$$\mathcal{A} = \frac{p_1}{p_2} + \frac{p_2}{p_1} + 2 \tag{7}$$

The energy range and the decay volume are defined to be the same as in the $\pi^0\pi^0$ mode. The small distance between the effective positions of the AKS converter and the AKS counter, (2.2 ± 0.1) cm is taken into account.

In the $\pi^+\pi^-$ mode, the distance scale depends only on the knowledge of the relative geometry of DCH1 and 2. Likewise, the uncertainty of the energy scale depends on the geometry, because the influence of the magnetic field uncertainty cancels in Eq. 6. The distance scale in the $\pi^+\pi^-$ event reconstruction can be checked, as in $\pi^0\pi^0$ decays, by comparing the position of the edge of the $K_S \to \pi^+\pi^-$ decay vertex distribution with the nominal position of the AKS counter. A small mismatch of 2.5 cm is found in the data corresponding to a shift in the distance of the two chambers of 2 mm or to a 20 μm relative transverse scale mismatch. Neither of the two can be excluded. A correction of $(2 \pm 2){\times}10^{-4}$, corresponding to a 2.5 cm distance scale change, is applied to the double ratio.

7.3 Background rejection and subtraction in the $\pi^0\pi^0$ sample

The background to the $\pi^0\pi^0$ signal comes uniquely from $K_L \to 3\pi^0$ decays. It is largely suppressed by requiring no additional showers within ± 3 ns around the event time. In order to avoid possible losses due to noise, only showers with reconstructed energy higher than 1.5 GeV are considered for this cut. This does not affect the suppression of $3\pi^0$ decays since, for kinematic reasons, very few photons with energy below 1.5 GeV coming from such decays can reach the LKr calorimeter. The remaining background consists of events with escaping or overlapping photons, resulting in only four reconstructed showers.

Further suppression is achieved by requiring that the χ^2 (Eq. 4) is less than 13.5, which corresponds to 3.7σ of the $m_{\gamma\gamma}$ resolution. The loss due to this cut is dominated by photon conversion and is $\sim$7%. The residual background is evaluated by comparing

the properties of the experimental data in the control region defined by $36 < \chi^2 < 135$ (Fig. 11), for both K_S and K_L decays, with the corresponding Monte Carlo distributions.

In the K_S beam, the 4-shower events contain almost exclusively $\pi^0\pi^0$ decays, and the χ^2 control region is populated by events which have an energy response or a shower coordinate displacement outside their normal Gaussian distribution. There are essentially two contributing processes. The first is a decay with a photon conversion (or a $\pi^0 \to ee\gamma$ decay) where just 4 showers are reconstructed in the calorimeter. Since no cuts are imposed against the presence of charged particle tracks, such events can end up as $\pi^0\pi^0$ candidates. Their χ^2 value can be very large and, correlated with it, there can be a displacement of the reconstructed kaon decay vertex relative to the original longitudinal position. The second contribution is the occurrence, in about 0.3% of showers, of hadronic photoproduction in their early stage of development in the liquid Krypton, with a consequent reduction of their reconstructed energy. Both types of processes, leading to non-Gaussian tails, are taken into account in an appropriate Monte Carlo simulation. The simulation traces the electron-positron pair through the spectrometer and, for the effects of hadronic photoproduction, makes use of the experimental data obtained in calibration runs with electrons. The Monte Carlo for K_S gives a good fit to the experimental χ^2 distribution over its full range, as well as to the distribution of the longitudinal decay vertex position for events in the χ^2 control region. On the other hand, the experimental χ^2 distribution for K_L clearly exceeds the one predicted by the (exclusively $2\pi^0$) Monte Carlo at high value of χ^2.

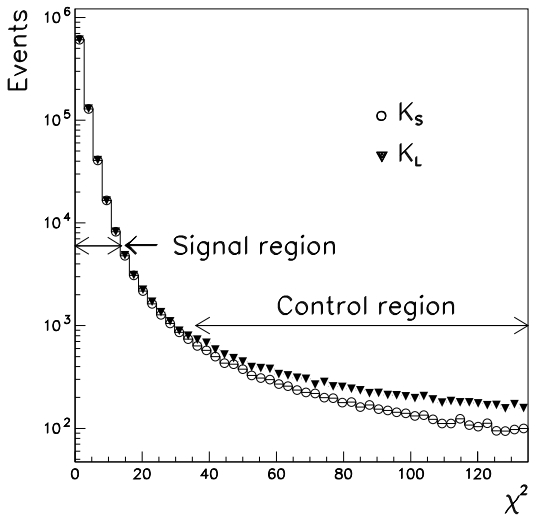

Figure 11: The comparison of the χ^2 distributions for K_L and $K_S \to 2\pi^0$ candidates, showing the excess due to the $3\pi^0$ background in the K_L sample.

The background from $3\pi^0$ decays populates, to a good approximation, the m_1-m_2 space evenly, owing to its combinatorial character. The χ^2 is defined such that each bin corresponds to an equal area in the m_1-m_2 plane, which allows an almost flat extrapolation into the signal region. An extrapolation factor of 1.2 ± 0.2 was derived from Monte Carlo simulation. This simulation, when normalised to the kaon flux, agrees with the background level extracted from the data.

The background is subtracted from the $K_L \to 2\pi^0$ sample in bins of kaon energy. The resulting correction on the double ratio, taking into account all uncertainties, is $(-5.9 \pm 2.0) \times 10^{-4}$.

7.4 Background rejection and subtraction in the $\pi^+\pi^-$ sample

7.4.1 K_S sample

In order to eliminate the background from $\Lambda \to p\pi^-$ in the $K_S \to \pi^+\pi^-$ sample, a cut is applied on the track momentum asymmetry,

$$\frac{|p_+ - p_-|}{p_+ + p_-} < \min(0.62, 1.08 - 0.0052E_K) \tag{8}$$

where E_K is the kaon energy in GeV. This cut is applied to both the K_S and the K_L samples, and its choice is motivated, apart from Λ rejection, by its improvement of the detector illumination symmetry. The residual Λ contamination was verified to be negligible by comparing the invariant $m_{p\pi}$ mass distributions of $K_S \to \pi^+\pi^-$ candidates, with $|m_{\pi\pi} - m_K|$ between 3 and 5 sigma of the $m_{\pi\pi}$ resolution, for opposite signs of the momentum asymmetry. Due to the large $\Lambda/\bar{\Lambda}$ production asymmetry (7/1), in case of Λ contamination, the two samples would show a significant difference in the population of this control region which is not observed.

7.4.2 K_L sample

In the $K_L \to \pi^+\pi^-$ sample, the two semi-leptonic K_L decay modes, K_{e3} and $K_{\mu 3}$, are the dominant background sources. The K_{e3} decays are suppressed by requiring E/p to be less than 0.8. $K_{\mu 3}$ decays are rejected when signals in the muon veto system, associated with the tracks, are found within 4 ns. Both cuts are also applied to K_S candidates in order to symmetrise losses of true $\pi^+\pi^-$ decays with a large electro-magnetic energy deposit (5.0%) or with a $\pi \to \mu\nu$ decay (1.3%).

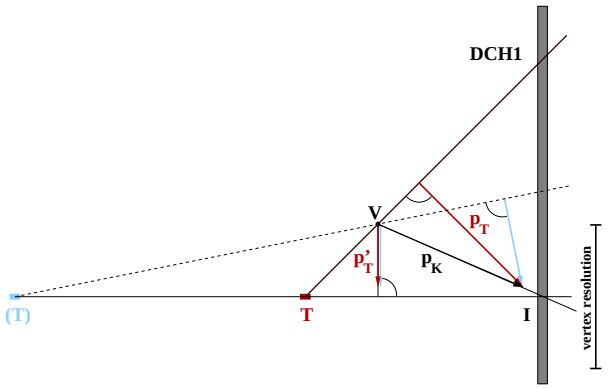

Figure 12: Principle of the transverse momentum calculation viewed in the plane defined by the reconstructed kaon momentum p_K and the target T; V is the decay vertex and I is the reconstructed kaon impact point at DCH1. For a vertex misplaced due to resolution, $p_T{}'$ remains independent of the target position.

Further elimination of the semi-leptonic channels is achieved by requiring the invariant mass $m_{\pi\pi}$ to be compatible with the kaon mass to within 3σ of the resolution, where the resolution is a function of the kaon energy. The cut on $m_{\pi\pi}$ also rejects all direct emission $\pi\pi\gamma$ decays [28], present only in the K_L beam. Most of the inner Bremsstrahlung decays are accepted; they are, however, K_S and K_L symmetric. This symmetry was tested by Monte Carlo simulation to hold to better than 10^{-4}.

The missing momentum carried away by the undetected neutrino in the semi-leptonic decays is reflected in p_T. The variable p_T is the transverse component of the

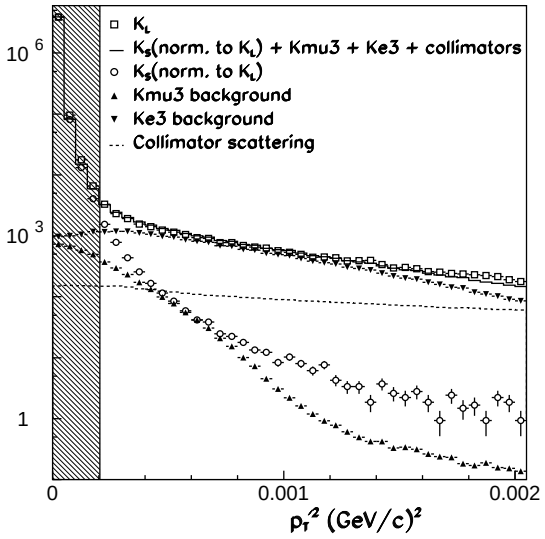

Figure 13: Comparison of the ${p_T}'^2$ tail of the $K_L \to \pi^+\pi^-$ candidates with the sum of all known components.

reconstructed kaon momentum p_K with respect to its flight direction, assuming that it comes from the target. The K_S or K_L target is chosen according to the vertical vertex position. To equalise the effect of the resolution of the vertex position reconstruction for K_S and K_L, the ${p_T}'$ component of the kaon momentum (Fig. 12) is chosen as a variable for background discrimination. This component is orthogonal to the line TI joining the target with the reconstructed kaon impact point at the DCH1. The relation between ${p_T}'$ and p_T is

$$ {p_T}' = \frac{TV}{TI} p_T \tag{9} $$

where TV is the distance from the target to the decay vertex. By requiring ${p_T}'^2$ to be smaller than 200 MeV^2/c^2, most of the semi-leptonic background remaining after the $m_{\pi\pi}$ cut is rejected, while $\pi^+\pi^-$ event losses are small (0.1%). The asymmetry between K_S and K_L due to non-Gaussian tails is smaller than 2×10^{-4}. This is included in the reconstruction uncertainty in Tab. 7.

In order to subtract the residual K_{e3} and $K_{\mu3}$ background, two control regions are defined in the $m_{\pi\pi}$-${p_T}'^2$ plane. The first region, $9.5 < (m_{\pi\pi} - m_K) < 19.0$ MeV/c^2 and $300 < {p_T}'^2 < 2000$ MeV^2/c^2, is dominated by K_{e3} events, while the second, $-17.0 < (m_{\pi\pi} - m_K) < -12.0$ MeV/c^2 and $300 < {p_T}'^2 < 500$ MeV^2/c^2, contains roughly equal numbers of K_{e3} and $K_{\mu3}$ events. Both regions are chosen such that they contain neither $\pi\pi\gamma$ events nor collimator scattered events (see section 7.5), and have sufficiently symmetric resolution tails in the K_S and K_L beams.

To model the background distributions in the control and signal regions, a K_{e3} sample is selected with $E/p > 0.95$, and a $K_{\mu3}$ sample is obtained by reversing the muon veto requirement. The latter contains also $\pi \to \mu\nu$ decays which are taken into account by comparison with a similarly selected K_S sample. The number of true $K_L \to \pi^+\pi^-$ decays in these regions is estimated from the $K_S \to \pi^+\pi^-$ sample. The $K_L \to \pi^+\pi^-$ candidates are compared to the model samples and the scaling factors that best match the two background model samples are found. Their extrapolation into the signal region gives a background estimate of 10.1×10^{-4} for the K_{e3} component, and 6.2×10^{-4} for $K_{\mu3}$. The

independence of the double ratio on the choice of control regions has been tested, and all results are compatible within $\pm 2 \times 10^{-4}$.

As a further check, the ${p_T}'^2$ distribution of $K_L \to \pi^+\pi^-$ candidates is compared over a large ${p_T}'^2$ interval with the sum of all contributing components (Fig. 13), taking into account kaon decays from collimator scattering. Deviations of around 10% were shown to come from events with high hit multiplicity. Their influence on the background estimate is reflected in an increased uncertainty on the amount of subtracted background.

The background subtraction is applied in bins of kaon energy and the overall correction on the double ratio is $(16.9 \pm 3.0) \times 10^{-4}$.

7.5 Collimator scattering correction

Both beams are surrounded by halos of particles from scattering in the collimators. Since the collimators are close to the decay region, the scattered particles manifest themselves through $K_S \to \pi\pi$ decays.

7.5.1 K_S beam

A beam halo in the K_S beam is formed by scattering in the collimator or in the AKS anti-counter. It is cut symmetrically in the $\pi^0\pi^0$ and $\pi^+\pi^-$ decay modes by requiring the radius of the centre of gravity (the distance of the virtual kaon impact from the beam axis), $C_g = \sqrt{C_{gx}^2 + C_{gy}^2}$, to be less than 10 cm. C_g is defined at the plane of the LKr calorimeter, where the two beams cross, and the cut is applied in all four modes. In the $\pi^0\pi^0$ mode, C_g is computed from the positions (x_i, y_i) and energies E_i of the four showers.

$$C_{gx}^{00} = \frac{\sum_1^4 x_i E_i}{E_K} \quad C_{gy}^{00} = \frac{\sum_1^4 y_i E_i}{E_K} \tag{10}$$

In the $\pi^+\pi^-$ mode, the positions (x_i, y_i) are obtained by extrapolating the track trajectories before the spectrometer magnet to the plane of the LKr calorimeter. The C_g resolutions are almost the same for $\pi^0\pi^0$ and $\pi^+\pi^-$ decays (Fig. 14a).

The value of the cut is chosen such that only a small part of the halo ($\sim$1% of all K_S events) is rejected. The acceptance differences between $\pi^+\pi^-$ and $\pi^0\pi^0$ decays are taken into account in the Monte Carlo, which contains a parametrised shape of the beam halo. The accuracy of the cancellation is verified by varying the centre of gravity cut, and the uncertainty is taken into account in the acceptance correction.

7.5.2 K_L beam

The K_L beam is defined and cleaned by three collimators. Double-scattered events dominate the beam tails. Unlike in the K_S beam, in the K_L beam, the ${p_T}'^2$ cut rejects more scattered events than the centre of gravity cut. The ${p_T}'^2$ cut is applied only to $\pi^+\pi^-$ decays; in $\pi^0\pi^0$ decays, the scattered events are removed only by the centre of gravity cut (Fig. 14b).

The correction for this asymmetry is computed from reconstructed $K_L \to \pi^+\pi^-$ candidates with an inverted ${p_T}'^2$ cut. The scattered events are identified by the $m_{\pi\pi}$ invariant mass, and the background continuum is subtracted (Fig 15). By extrapolating the computed kaon trajectory back to the planes of the final or cleaning collimator, rings having the collimator radii can be seen. This demonstrates the origin of these events. Scattered events have a 30% higher probability of containing an accompanying shower

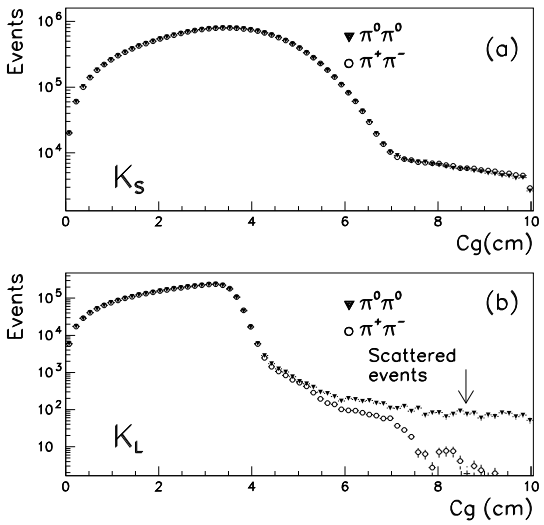

Figure 14: Radial distributions of the centre of gravity for K_S and K_L beams after all cuts.

not associated to the track than the decays of kaons coming from the target. Since such events are rejected in the $\pi^0\pi^0$ selection, this factor has to be taken into account in the correction. The correction is applied in bins of energy and it amounts to $-(9.6\pm2.0)\times10^{-4}$. The error is dominated by the uncertainty on the accompanying shower factor.

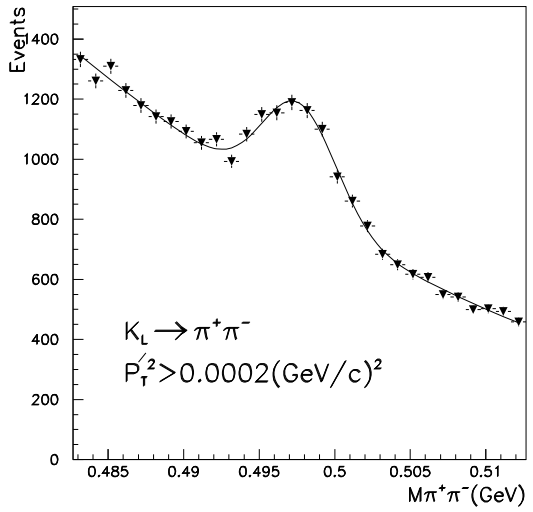

Figure 15: Collimator scattered events at $p_T{}'^2 > 200$ MeV^2/c^2.

One cross-check of this result involves searching for scattered events in the $\pi^0\pi^0$ sample with centres of gravity between 5 and 10 cm. This region is also populated by $3\pi^0$ background, and by decays from kaons scattered in the defining collimator, which are confined to low transverse momenta. A combination of the three contributions is fitted to the centre of gravity distribution of $K_L \to 2\pi^0$ candidates. The model distributions of scattered events are obtained from $\pi^+\pi^-$ decays, and the shape of the $3\pi^0$ background is obtained from events with high χ^2, cross-checked with 5-shower events.

A second cross-check consists of looking at the proper time distribution of events with centre of gravity between 5 and 10 cm (Fig. 16). The scattered events follow the

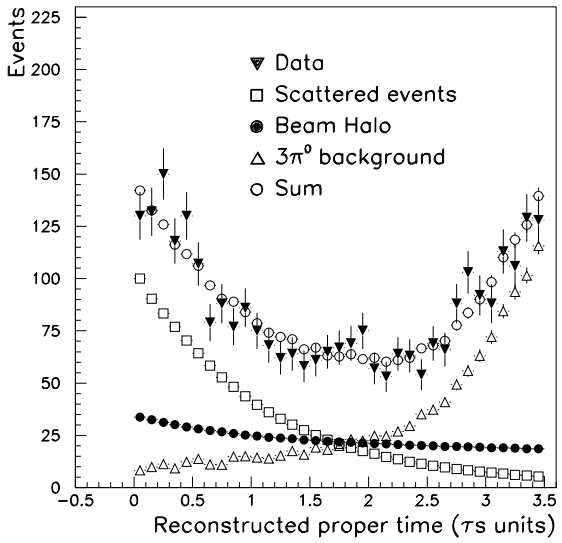

Figure 16: Direct determination of the number of collimator scattered events in the $K_L \to \pi^0\pi^0$ sample with $5 < C_g < 10$ cm from the proper time distribution.

falling K_S decay curve, whereas the $3\pi^0$ background increases at the end of the decay volume. In addition, the distribution of events scattered at the defining collimator, which are a mixture of K_L and K_S decays, was simulated using the collimator geometries.

All three methods give compatible results within the uncertainty of the correction.

8 K_S tagging

To associate an event with its parent beam, information from the tagging station, which records the protons that produce K_S particles, is used. A decay is labelled K_S if a coincidence is found between its event time and a proton time measured by the Tagger. The good time resolutions inherent to the detectors guarantee accurate identification. Fig. 17 shows the tagging distributions for K_S and K_L decays to $\pi^+\pi^-$ which have been identified as such by their vertex position in the vertical plane. A similar procedure is not possible for neutral decays. Tagging is therefore the only tool available to distinguish K_S from K_L. The selection of K_S and K_L samples is done by means of tagging for both the $\pi^+\pi^-$ and $\pi^0\pi^0$ modes, so that the uncertainties are kept symmetric. Two kinds of mistagging can occur:

– A K_S decay can be assigned to the K_L beam. This probability is due to coincidence inefficiencies and it is denoted by α_{SL}. These inefficiencies are small ($\sim 10^{-4}$), but they might differ for $\pi^+\pi^-$ and $\pi^0\pi^0$ decays because the respective event times are reconstructed from different detectors.

– A K_L decay can be identified as K_S. This is due to accidental coincidences between the event and proton times, and it is denoted as α_{LS}. This probability only depends on the proton rate in the Tagger, so, to first order, it affects both $\pi^+\pi^-$ and $\pi^0\pi^0$ decays equally. It is $\sim 10\%$ for the chosen coincidence window.

Both mistagging fractions vary according to the width of the coincidence window. The tagging window used in this analysis, ± 2 ns, was chosen to minimise the total uncertainty on R that comes from mistagging.

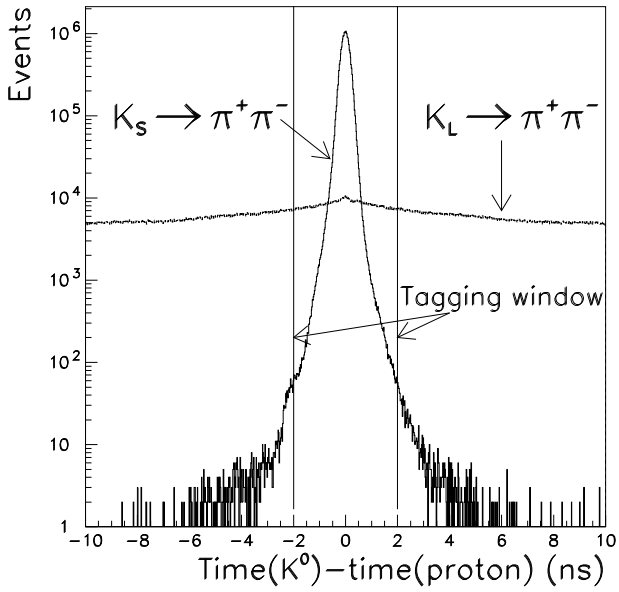

Figure 17: Time coincidence for charged K_S and K_L events, identified by their reconstructed vertex.

8.1 K_S tagging inefficiency: α_{SL}

The tagging inefficiency can be measured accurately in the charged mode, because the identification of the decay origin is possible from the vertex reconstruction. In identified K_S decays, a fraction of $(1.63 \pm 0.03) \times 10^{-4}$ lies outside the defined ± 2 ns coincidence window, as shown in the distribution of the difference between the event time provided by the hodoscope and the closest proton time (Fig.17). Redundant time information provided by the drift chambers demonstrates that $\sim$80% of these tails are due to Tagger inefficiencies. The reconstruction inefficiency of the hodoscope time is responsible for the remaining $\sim 3 \times 10^{-5}$. Since mistagging is predominantly due to the Tagger itself, it affects equally $\pi^0\pi^0$ and $\pi^+\pi^-$ modes, so that its effect cancels in the double ratio.

In order to measure the part of the inefficiency associated with the neutral time reconstruction, a large sample of K_S and K_L decays into $2\pi^0$ and $3\pi^0$ is used, where one of the photons converts into an electron-positron pair. The usual selection and quality criteria are applied, but without requiring the reconstruction of the complete decay. Accepted events are allowed to contain between four and seven clusters. The two tracks must cross to give a vertex and must fulfill the electron identification hypothesis, i.e. $E/p > 0.95$. The charged time is computed using the standard procedure applied to the two electron tracks. The neutral time is computed by the association of central and lateral cell times of all electro-magnetic showers satisfying some weak criteria which ensure that they belong to a single event. The event-by-event compatibility of the charged and neutral time is checked within the usual ± 2 ns window (Fig. 18).

The number of cases where the two time measurements differ by more than 2 ns corresponds to the differential inefficiency associated with hodoscope and calorimeter time reconstruction. Including the sensitivity of the neutral time computation to the number and to the energy of photons in the systematic uncertainty, one finds that the tails in the time estimator difference Δt are less than 2.5×10^{-5} at a 68% confidence level. The same data sample allows the precise determination of the absolute value of the neu-

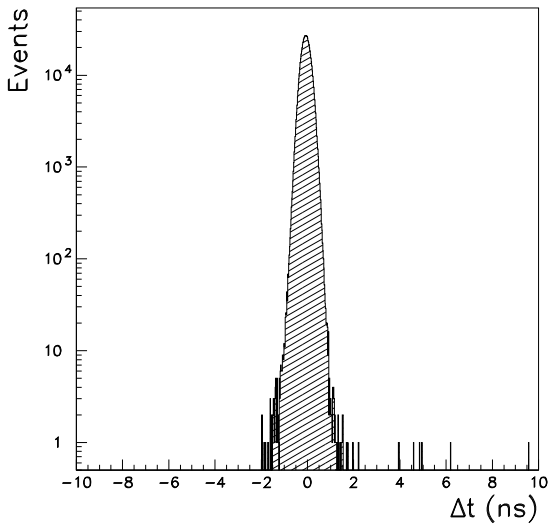

Figure 18: Difference Δt between charged and neutral time estimators for neutral decays with a conversion.

tral tagging inefficiency. Convoluting the neutral-charged time difference with the $\pi^+\pi^-$-$-$Tagger time difference, the tagging inefficiency for $\pi^0\pi^0$ is obtained. This inefficiency of $(1.64\pm0.5)\times10^{-4}$, has been found to be in good agreement with a direct evaluation determined in single K_S beam, where all events are associated with a proton. A third method consists of checking the neutral tagging inefficiency in an identified $K_S \to 2\pi^0$ sample belonging to the main data set. For this, $\pi^0\pi^0$ data are used with a subsequent $\pi^0 \to ee\gamma$ Dalitz decay. The vertex position reconstructed from the electron and positron tracks allows K_S decays to be selected. All events outside the $\pm$ 2ns coincidence window correspond to Tagger or calorimeter reconstruction inefficiencies. The result is in good agreement with the two methods described previously, though it remains statistically limited because of the small (1.2%) Dalitz branching ratio. Tab. 2 summarises the results on $\pi^0\pi^0$ tagging inefficiency.

Table 2: Different evaluations of K_S tagging inefficiency for $\pi^0\pi^0$ events.

Method	$\boldsymbol{\alpha_{SL}^{00}}$ **in** $\mathbf{10^{-4}}$
Conversions	1.64 ± 0.5(stat+syst)
Single $\boldsymbol{K_S}$ **beam**	1.90 ± 0.42(stat)
$\boldsymbol{\pi^0\pi^0}$ **with Dalitz**	$1.9^{+1.0}_{-0.8}$(stat)

The important consideration for the double ratio measurement is the mistagging difference between the charged and neutral modes. From the previous analyses, it can be concluded that there is no measurable effect within an uncertainty of $\pm0.5\times10^{-4}$.

8.2 Accidental tagging: α_{LS}

Because of the high rate in the Tagger, K_L events can have an accidental coincidence with a proton. The probability for this to happen is proportional to the width of the tagging window. It can be measured directly in charged decays by looking at the fraction of those $\pi^+\pi^-$ events identified from their vertex position as K_L decays, that also have a proton in the $\pm$2 ns time window (Fig. 19a). On average, it was found that

$\alpha_{LS}^{+-} = (10.649 \pm 0.008)\%$. Such a direct evaluation is not possible for neutral events. An indirect method is therefore applied to both the $\pi^+\pi^-$ and the $\pi^0\pi^0$ modes, to evaluate the quantity $\Delta\alpha_{LS} \equiv \alpha_{LS}^{00} - \alpha_{LS}^{+-}$, which leads to a correction to the double ratio. The K_L samples were identified as such by tagging, so that no proton is detected within ± 2 ns of the event time. With this sample, the quantity β_{tag} is computed, which is the probability of having a proton within a ± 2 ns sideband window, located before or after the event time (Fig. 19b). These windows are centred at 5 ns intervals from the event time, and so follow

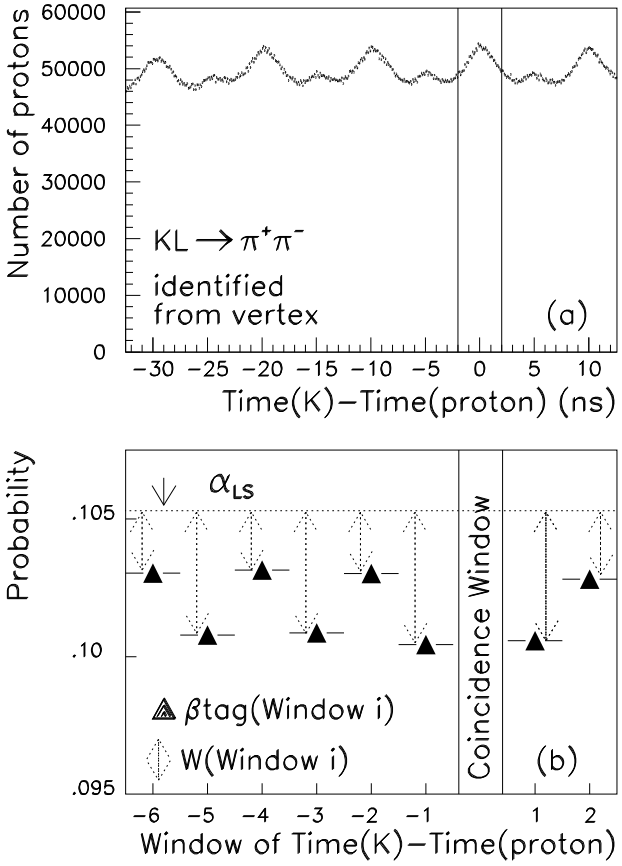

Figure 19: (a) The distribution of proton times with respect to event time for $K_L \to \pi^+\pi^-$ identified from vertex. (b) The variables α_{LS}, β_{tag} and W are schematically shown for $K_L \to \pi\pi$ tagged events.

the 200 MHz structure of the proton beam. Because β_{tag} is measured using the fraction of K_L events without an accidental coincidence in the central window, the proton rate is generally slightly lower than for the full sample. This is reflected in β_{tag} being smaller than α_{LS} by a quantity W. Typically, W is $\sim$10% of α_{LS}. Mainly due to the 100 MHz beam structure, β_{tag} varies with the window; however, the corresponding W value compensates for this, using the relation:

$$\alpha_{LS}^{00} - \alpha_{LS}^{+-} = (\beta_{tag}^{00} + W^{00}) - (\beta_{tag}^{+-} + W^{+-})$$

The β_{tag} parameters are extracted from the same data that are used for the double ratio determination. In the $\pi^+\pi^-$ mode, W^{+-} can be computed by comparing α_{LS}^{+-} and β_{tag}^{+-} in all windows, using the K_L sample identified by vertex position. In a similar way, β_{tag}^{00} can be extracted. To measure W^{00}, the assumption is made that $K_L \to 2\pi^0$ and $K_L \to 3\pi^0$

decays are tagged identically, giving $W^{00} = W^{000}$. The abundant sample of $K_L \to 3\pi^0$ decays is then used to derive W^{00}. Finally, in order to increase the statistical significance of the measurements, several 4 ns wide windows are used in the sideband region. The results are shown in Tab. 3:

Table 3: Measured values of parameters $\Delta\beta_{tag}$, ΔW and $\Delta\alpha_{LS}$.

	Units of 10^{-4}
$\boldsymbol{\Delta\beta_{tag} = \beta_{tag}^{00} - \beta_{tag}^{+-}}$	3.0 ± 1.0(stat)
$\boldsymbol{\Delta W = W^{00} - W^{+-}}$	1.3 ± 1.1(stat)
$\boldsymbol{\Delta\alpha_{LS} = \alpha_{LS}^{00} - \alpha_{LS}^{+-}}$	4.3 ± 1.4(stat) ± 1.0(syst)

The quoted systematic error on $\Delta\alpha_{LS}$ takes into account the small variation of the result depending on the set of out-of-time windows used in the computation. Several arguments support the assumption $W^{00} = W^{000}$. Firstly, the trigger conditions for $K_L \to 2\pi$ and $K_L \to 3\pi^0$ are similar and highly efficient ($\sim$99.9%). Secondly, these two modes are reconstructed by the same detector with similar criteria. Finally, in 2000, a special run period was devoted to measure simultaneously both W^{00} and W^{000}. After passing through the Tagger, the K_S proton beam was deviated away from the trajectory leading to the K_S target, so that only particles from the K_L beam decayed in the fiducial region. All the tagging parameters analysed show good compatibility between the $2\pi^0$ and $3\pi^0$ modes. In particular it is found:

$$W^{00} - W^{000} = (-0.8 \pm 2.9)\times 10^{-4}$$

which confirms the initial assumption. Even though there is an overall agreement of the tagging parameters between the $2\pi^0$ and $3\pi^0$ modes, β_{tag}^{00}, which is the largest part of α_{LS}^{00}, is directly measured from the sample entering in the double ratio, namely $2\pi^0$ events. The usage of the external $3\pi^0$ sample is restricted to the determination of the W^{00} parameter only.

8.2.1 Origins of $\Delta\alpha_{LS} \neq 0$

The measured difference $\Delta\alpha_{LS} = (4.3 \pm 1.8)\times 10^{-4}$ (see Tab.3) indicates that the $\pi^0\pi^0$ and $\pi^+\pi^-$ samples are recorded in conditions of slightly different intensities, although the same rejection of trigger dead time and drift chamber overflow is applied to both modes. The reason for this is the higher sensitivity to accidentals in the trigger conditions and reconstruction of $\pi^+\pi^-$ compared to $\pi^0\pi^0$. The first contribution to $\Delta\alpha_{LS}$, associated with $\pi^+\pi^-$ events lost at the trigger, is $(1.0 \pm 0.3)\times 10^{-4}$. This has been verified studying events collected with fully relaxed trigger. The second contribution, related to the event losses at the reconstruction, is studied superimposing good events from data or simulation to beam monitor triggers, recorded in proportion to the intensity (see section 10.1.1), and it is $(2.5 \pm 0.4)\times 10^{-4}$.

Tab. 4 shows the comparison between expected and measured $\Delta\alpha_{LS}$ values for the available data samples. It is noted that improvements in the $\pi^+\pi^-$ trigger code and the lower instantaneous intensity allowed by a longer spill, result in a smaller loss for charged decays and consequently in a smaller $\Delta\alpha_{LS}$ in 1999 relative to 1998 data. The measured values of $\Delta\alpha_{LS}$ and their variation between the two years agree well with the expectations within errors.

Table 4: Values of $\Delta\alpha_{LS}$ in the two different data periods, and comparison with the expectations from known sources.

Data Sample	**Expected $\Delta\alpha_{LS}$ Units of 10^{-4}**	**Measured $\Delta\alpha_{LS}$ Units of 10^{-4}**
1998	5.1±1.0	8.3±2.9
1999	2.6±0.6	2.6±2.1
1998+1999	3.5±0.5	4.3±1.8

8.3 Effect of the K_S tagging on R

After all cuts, four event samples remain, namely $\pi^+\pi^-$ and $\pi^0\pi^0$ events tagged as K_S, and $\pi^0\pi^0$ and $\pi^+\pi^-$ events tagged as K_L. The mistagged fraction of events is subtracted from K_S and added to K_L. The double ratio is then sensitive to $\Delta\alpha_{SL}$ and $\Delta\alpha_{LS}$:

$$\Delta R \approx -6(\alpha_{SL}^{00} - \alpha_{SL}^{+-}) \quad \Delta R \approx 2(\alpha_{LS}^{00} - \alpha_{LS}^{+-})$$

where the numerical factors depend on the absolute mistagging probability α_{LS} and on the flux ratio K_S/K_L. The corresponding corrections to the double ratio become:

$$\Delta R = (0.0 \pm 3.0)\times 10^{-4} \text{ for } \Delta\alpha_{SL}$$
$$\Delta R = (8.3 \pm 3.4)\times 10^{-4} \text{ for } \Delta\alpha_{LS}$$

9 Acceptance correction

K_S and K_L particles decay with very different lifetimes. Despite the use of a common decay region of $3.5\tau_S$, the decay distributions vary strongly along the beam direction. The resulting acceptance correction on R can reach about $\pm 10\%$, depending on the kaon energy. To cancel the contribution from the different lifetimes to the acceptance, the K_L distributions are weighted by a factor $W(\tau)$, where τ is the proper time of the kaon:

$$W(\tau) = \frac{I(\tau \text{ from } K_S \text{ target}) \to 2\pi}{I(\tau \text{ from } K_L \text{ target}) \to 2\pi}$$

$I(\tau)$ describes the complete kaon decay intensity into 2π, containing K_S, K_L and interference components:

$$I(\tau) = \mathrm{e}^{-\tau/\tau_S} + |\eta|^2 \mathrm{e}^{-\tau/\tau_L} + 2|\eta|\mathrm{D_p}\mathrm{e}^{-\frac{1}{2}\tau(1/\tau_L+1/\tau_S)}\cos(\Delta M\tau - \phi)$$

For the kaon system decay parameters τ_S, τ_L, ΔM, η and ϕ, the world averages given in the Particle Data Book [29] were used. The K^0-$\overline{K}^0$ production asymmetry factor $\mathrm{D_p}$ is obtained by a fit to the data, in an energy range $E_K \geq 120$ GeV where the interference term is significant. After weighting, the K_L and K_S decay distributions become nearly identical, as shown in Fig. 20. The few K_S events reconstructed upstream of the AKS are due to resolution while in the K_L case the applied cut at τ_S=0 defines the beginning of fiducial region. A small difference in acceptances remains, related to the difference in K_S and K_L beam sizes and directions. This residual correction is computed using a large-statistics Monte Carlo simulation.

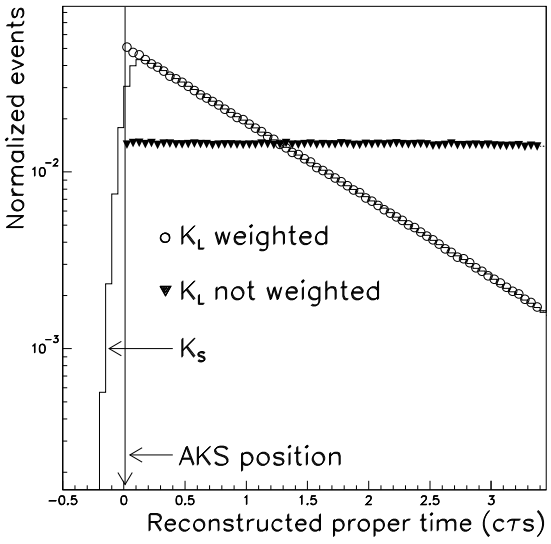

Figure 20: Reconstructed lifetime distribution for $K_L \to \pi^+\pi^-$ events before and after weighting.

By adopting the proper-time weighting method, the K_L statistics effectively decrease and, within the fiducial region of $3.5\tau_S$, it results in a $\sim$35% increase in the statistical error of R.

9.1 Simulation tools

The Monte Carlo precisely simulates the K^0 beams and detector apertures. The simulation of the K_L beam includes the K_S component and the interference term, using the measured production asymmetry factor $\mathrm{D_p}$. Particle interactions in the detector material are parametrised. The effect of kaon scattering and neutron interaction in the K_S collimator and the K_S anti-counter are included in the Monte Carlo by parametrising an energy dependent K_S beam halo, which reproduces well the experimental distributions of the centre of gravity for $\pi^+\pi^-$ and $\pi^0\pi^0$ modes. The measured wire inefficiencies are introduced before the event reconstruction. To describe the photon response in the calorimeter, a library containing 1.7×10^5 showers is used, generated using GEANT in 36 energy bins from 2–101 GeV in order to guarantee good resolution and linearity and in a large 51×51 cell area to allow realistic energy sharing for close particles. A parametrisation of the non-Gaussian tails is added to the photon energy, together with the measured electronic noise and known contributions from non-uniform response. Two other libraries are used: one for electrons to describe conversions or Dalitz decays, and another for charged pions.

To obtain an accurate acceptance correction, 3×10^8 kaon decays per mode were generated. After all cuts, statistics equivalent to five times the data were obtained. The generation is sub-divided into run periods that follow the spectrometer magnetic field direction, the beam position in the detectors, dead cells in the calorimeter and wire problems, as they are observed in the data. Simulated events undergo standard reconstruction and analysis criteria.

9.2 Correction on the double ratio and systematic checks

The effect of the acceptance on the double ratio, as obtained from Monte Carlo, is shown in Fig. 21 in 5 GeV kaon energy bins. It is used to derive the acceptance correction.

For comparison, the acceptance effect without applying proper time weighting to the K_L events is also shown.
The largest contribution to the correction comes from the difference between the K_S and K_L beams around the beam axis in the spectrometer for $\pi^+\pi^-$ decays. The acceptance correction related to the $\pi^0\pi^0$ mode is small. The illumination of the calorimeter for

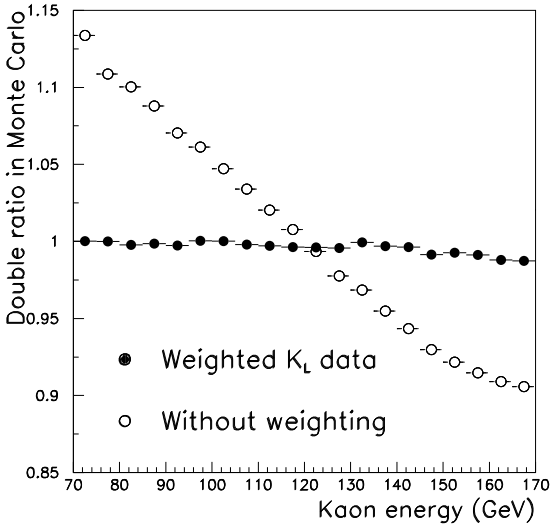

Figure 21: Acceptance effect to the double ratio R as computed from Monte Carlo, in kaon energy bins. The case without weighting K_L data is also shown.

$\pi^+\pi^-$ and $\pi^0\pi^0$ decays is shown in Fig. 22, in a comparison for K_S and weighted K_L events. The K_S/K_L ratio varies in the $\pi^+\pi^-$ mode for track positions close to the beam tube (Fig. 22.b). This is reproduced by the simulation, so the effect is absorbed into the acceptance correction. In the $\pi^0\pi^0$ mode, the photon distribution in the calorimeter is almost identical for K_S and weighted K_L events, as shown in Fig. 22.d.

The systematic uncertainties are evaluated by modifying certain parameters until the agreement between experimental and simulated distributions is affected. Varying the K_S beam halo, the K^0-$\overline{K^0}$ production asymmetry, the beam shapes in the detectors and the wire inefficiencies, the correction is stable to within 3.3×10^{-4}. A systematic cross-check was done by sending the generated kinematic values of all 3×10^8 events per mode of the Monte Carlo through a GEANT based Monte Carlo in order to identify biases associated to the fast simulation. Within the statistical accuracy, no difference was observed in the neutral mode. In the charged mode, an event-by-event comparison showed a systematic difference of $(-4.6 \pm 2.3)\times10^{-4}$.

While the effect is small, the average of the two evaluations, with a systematic error increased by 2.3×10^{-4}, is conservatively quoted as an acceptance correction. The final correction to R for the acceptance is:

$$\Delta R(\text{acceptance}) = (+26.7 \pm 4.1(\text{stat}) \pm 4.0(\text{syst}))\times10^{-4}$$

10 Effects related to beam activity and detector response variations

The identification of good $K \to \pi\pi$ decays might be affected by the presence of extra activity from various sources. Additional particles can either be produced simultaneously with the kaon candidate in the target (called 'in-time'), or they can come from

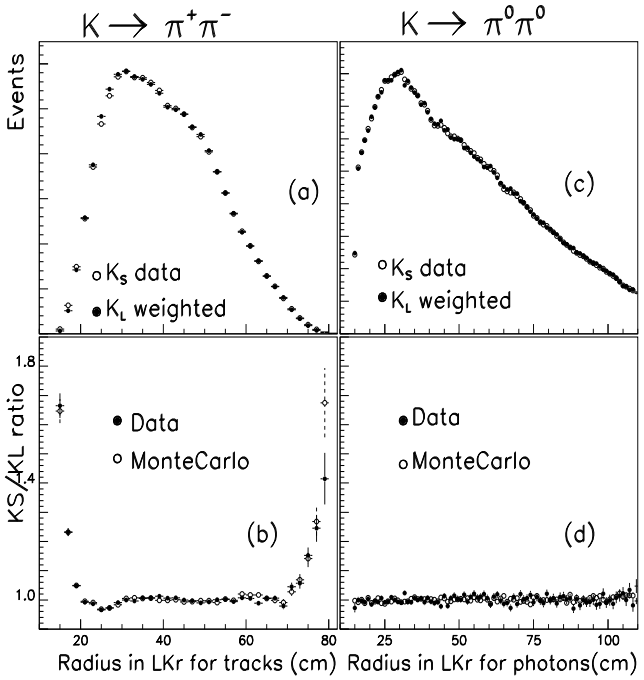

Figure 22: The calorimeter illumination by $\pi^+\pi^-$ tracks for K_S and K_L weighted events is shown in (a), while the K_S/K_L ratio for data and MC is shown in (b). Similarly, the calorimeter illumination for photons as a function of the radius for $\pi^0\pi^0$ is shown in (c), with the K_S/K_L ratio for data and MC shown in (d). Distributions are shown for events in the kaon energy range 95-100 GeV.

uncorrelated kaon decays (called 'accidentals'). Accidental particles come mainly from the intense K_L beam, and the neutron and muon components accompanying it. In-time background is effectively suppressed for K_L decays given the beam collimation and the extensive shielding, while in the K_S beam a possible additional in-time component needs to be considered. Beam intensity variations do not affect the double ratio, thanks to the concurrent recording of all four modes. However, slow variations of the K_S/K_L intensity during the run that accidentally coincide with unaccounted variations in the charged-to-neutral event ratio (e.g. from a change in the detector response), would lead to a bias. The measured variance of the K_S/K_L intensity ratio is $\sim$9%, while the $\pi^+\pi^-/\pi^0\pi^0$ ratio, corrected for trigger inefficiency, varied by 1–2% during the 1998-1999 data period. The potentially resulting effect is taken into account in the analysis by weighting the K_S events by a factor extracted from K_S/K_L intensity variation monitoring. The effect of this weighting on R is small ($\leq 3\times10^{-4}$), indicating that both the beams and the detectors were sufficiently stable during the two years of data taking.

10.1 Accidental activity

The pile-up of extra particles with a good event may result in an event loss, depending on the time and space separation in the detector. Owing to the simultaneous data taking, K_S and K_L events are equally sensitive to the accidental beam activity, to first order. A residual effect on R can be written as:

$$\Delta R = (\Delta R)_{\text{intensity}} + (\Delta R)_{\text{geometry}} \tag{11}$$

The two terms have the following origins:

1. **The intensity term**, $(\Delta R)_{\text{intensity}}$, appears if there is a decorrelation between the two beams. Describing the K_S and K_L beam intensity time dependences as $\mathrm{I}_{S,L}(\mathrm{t})= \langle \mathrm{I}_{S,L} \rangle \times (1+\eta_{S,L}(\mathrm{t}))$, this would mean that $\eta_S(\mathrm{t})$ and $\eta_L(\mathrm{t})$ differ. If in addition the mean $\pi^+\pi^-$ and $\pi^0\pi^0$ losses (λ^{+-} and λ^{00} respectively) are not equal an effect on the double ratio can be expected. Assuming that losses depend linearly on the beam intensity this effect is given by:

$$(\Delta R)_{\text{intensity}} = (\lambda^{+-} - \lambda^{00}) \times \langle \eta_L(\eta_L - \eta_S) \rangle \tag{12}$$

2. **The illumination term**, $(\Delta R)_{\text{geometry}}$, is non-zero if accidental losses depend on the detector illumination, since the latter is slightly different for the K_S and K_L beams. This can influence the double ratio if it is not equal for $\pi^0\pi^0$ and $\pi^+\pi^-$ events. The corresponding effect can be expressed as:

$$(\Delta R)_{\text{geometry}} = (\delta\lambda^{+-} - \delta\lambda^{00}) \times (1 + \langle \eta_L \eta_L \rangle) \tag{13}$$

where $\delta\lambda$ represents the difference in losses between the K_S and K_L beams.

The measurement of event losses induced by extra activity is necessary for evaluating these terms. This is done through the overlay method.

10.1.1 Overlay method

Losses from accidental activity can be simulated by overlaying data with special beam monitor (BM) triggers. Beam monitors (see section 5.3) trigger in proportion to the K_S and K_L beam intensities, so that the BM triggers give a picture of the ambient activity and noise measured by the detectors at a given time. Detector information for the event and the BM trigger are superimposed, and the so-called overlaid event undergoes the usual reconstruction. For this purpose only BM triggers without DCH overflow condition are used. After applying the standard analysis procedure, the probability of losing or gaining an event is computed by comparing, event-by-event, the original and overlaid samples. This method allows the effect of the extra activity and noise that was present when the data was recorded to be reproduced and measured. However, the method depends on how well the BM trigger content describes the intensity variations seen by the data. A comparative study of the extra activity in BM triggers and kaon events showed an agreement that was better than 97%.

To overcome the problem of doubling the detector noise in the overlaid event, leading to an overestimation of the losses, an alternative method is used in parallel: the overlaid Monte Carlo (OMC). This consists of using the BM triggers to overlay noiseless Monte Carlo events, instead of overlaying data. A small fraction of Monte Carlo events were overlaid consecutively with two different BM triggers (doubly overlaid Monte Carlo, or DOMC), in order to allow a direct comparison with the losses computed from overlaid data.

With these methods, two sources of losses and gains for good events were identified:

– The mortality due to a BM trigger. A BM trigger containing extra activity has an enhanced probability of killing an event in the overlay procedure. The extra activity depends on the beam intensity. Because of the different selection criteria, this would affect the $\pi^+\pi^-$ and $\pi^0\pi^0$ modes asymmetrically. Examples of cuts sensitive to the intensity include the muon veto in $\pi^+\pi^-$ and the rejection of extra photon clusters in $\pi^0\pi^0$.

– Noise in a detector. An event can be lost or gained after the overlay owing to migration across cut boundaries. Certain selection criteria are sensitive to noise, like the χ^2 distribution in $\pi^0\pi^0$. Losses caused by noise do not depend on the beam intensity.

The overall effect of the overlay is dominated by losses. The net effect of the overlay (losses minus gains) is shown in Tab. 5. OMC describes the reconstruction losses due to accidental activity and noise. Losses in the charged mode are dominated by the DCH multiplicity overflow condition, while in the neutral mode the χ^2 cut accounts for the bulk of the losses. Results obtained by comparing DOMC and OMC are directly comparable to those from the overlaid data. The agreement is reasonable in the $\pi^0\pi^0$ mode. DOMC gives slightly fewer losses in the $\pi^+\pi^-$ mode. This is associated with the smaller DCH multiplicity condition rate in DOMC.

Table 5: Net effect of accidental activity, computed using data and Monte Carlo events overlaid with BM triggers.The LKr noise effect is subtracted. The DOMC column represents differences between first and second overlay.

Losses–Gains	OMC	DOMC	Data overlay
$\boldsymbol{\pi^0\pi^0}$	0.8%	1.5%	1.4%
$\boldsymbol{\pi^+\pi^-}$	1.8%	2.5%	2.8%
$\boldsymbol{\pi^+\pi^- - \pi^0\pi^0}$	1.0%	1.1%	1.4%

In order to explore the losses throughout the entire range of beam intensity, information from the beam monitor, placed at the end of the beam tube, is used. In Fig. 23, the net accidental effect, computed from OMC, is shown for $\pi^+\pi^-$ and $\pi^0\pi^0$ events as a function of the recorded intensity at the time of the BM trigger used for the overlay. Losses increase faster in $\pi^+\pi^-$ than in $\pi^0\pi^0$ events. The overall behaviour is compatible with the assumption that the dependence of accidental losses with the rate is linear.

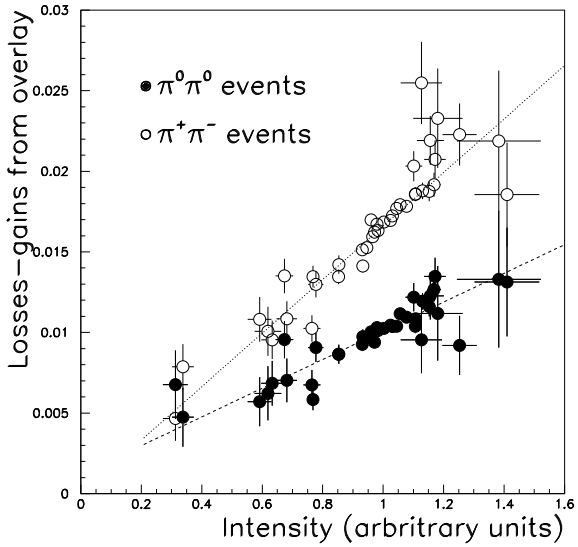

Figure 23: Losses as a function of the intensity seen by the BM trigger, computed by the overlay method. Lines are plotted to guide the eye.

In what follows, the conservative value computed from data overlay is assigned

to the difference of the effect of accidental activity on $\pi^+\pi^-$ and $\pi^0\pi^0$ events, namely $\lambda^{+-} - \lambda^{00} = (1.4 \pm 0.7)\%$.

10.1.2 Effect on the Double Ratio

Having measured the accidental losses for $\pi^+\pi^-$ and $\pi^0\pi^0$ events, the two terms of Eq. 11 can be computed. The intensity variation term, $(\Delta R)_{\text{intensity}}$, depends upon how well the variations of the two beams (η_S, η_L) mimic one other, as well as upon the differential losses between the $\pi^+\pi^-$ and $\pi^0\pi^0$ modes $(\lambda^{+-}, \lambda^{00})$, according to Eq. 12. Several estimators have been used to study a possible difference in the activity of the two beams, based on accidental information in good events. Among these are the number of hits in the AKL counters, the number of accidental clusters in the LKr calorimeter, and the number of extra tracks, all of which have been measured in both K_S and K_L events. The corresponding occurrence rates for these estimators are similar in the two beams. An independent method to measure the difference involves examining the correlation between the K_S and K_L beams. All results agree that, to within 1%, there is no intensity difference seen by K_S and K_L events. So from Eq. 12 we obtain $(\Delta R)_{\text{intensity}} = \pm 3 \times 10^{-4}$, where an additional, conservative factor of two is used in the uncertainty, to account for a possible non-linear dependence of losses with the intensity.

The illumination term, $(\Delta R)_{\text{geometry}}$, is estimated by the overlay method with data or Monte Carlo events. Both computations agree that there is no significant effect within available precision. The interpretation of the result is that all sources of losses are uniformly distributed in the acceptance. An upper bound on the illumination term can be quoted, according to the statistical significance of the measurement, namely $(\Delta R)_{\text{geometry}} = \pm 3 \times 10^{-4}$. Finally, the uncertainty on the double ratio from accidental activity is:

$$\Delta R = (\Delta R)_{\text{intensity}} + (\Delta R)_{\text{geometry}} = \pm 4.2 \times 10^{-4}$$

10.2 In-time activity

Particles produced in the K_L target, in time with the K_L are well suppressed by the 120 m of collimation and magnets. In the K_S case, the 6 m collimator occasionally allows in-time particles to survive into the decay region, and to be detected together with a good kaon decay.

To put bounds on such effects, the $\pi^0\pi^0$ sample accumulated in single K_S runs is used. The low intensity of the K_S beam ensures the absence of accidental particles. The $\pi^0\pi^0$ mode was chosen for the clean identification of the number of in-time clusters; in the charged mode, the extended and irregular hadronic showers could bias the study. By removing the extra (in-time) cluster cut, the $\pi^0\pi^0$ signal is enriched with the following events: $\pi^0\pi^0$ events which have a photon conversion, giving 5-cluster final modes and $\pi^0\pi^0$ events with additional in-time particles. Only in the case of photon conversion is the reconstructed χ^2 deteriorated. By comparing the experimental χ^2 distribution of $2\pi^0$ events with five clusters to the one predicted by Monte Carlo solely for conversions, an excess of $(0.7 \pm 0.4) \times 10^{-4}$ was found. This would correspond to the in-time activity, and has been cross-checked using various time windows for the extra-activity. Therefore, an upper bound on the in-time contamination in the K_S beam can be set to 1×10^{-4}. This is included in the uncertainty on accidental activity in Tab. 7.

Table 6: Number of selected events after accounting for mistagging.

	Statistics in millions		
	1998	1999	total
$K_L \to \pi^0\pi^0$	1.047	2.243	3.290
$K_S \to \pi^0\pi^0$	1.638	3.571	5.209
$K_L \to \pi^+\pi^-$	4.541	9.912	14.453
$K_S \to \pi^+\pi^-$	6.910	15.311	22.221
Statistical error	18.0×10^{-4}	12.2×10^{-4}	10.1×10^{-4}

11 Result

The number of events passing all selection criteria, taking into account K_S mistagging, is shown in Tab. 6 and their energy distribution in Fig. 24. The final result is computed by dividing the data into 20 bins of kaon energy from 70 to 170 GeV, and calculating the double ratio for each bin using proper-time weighted K_L samples. All corrections are applied to each bin separately, and the results are averaged. In order to avoid a statistical bias, instead of the simple weighted mean, the bins are averaged using a statistically unbiased logarithmic estimator. The average effects of the corrections on the raw double ratio, together with their uncertainties, are summarised in Tab. 7.

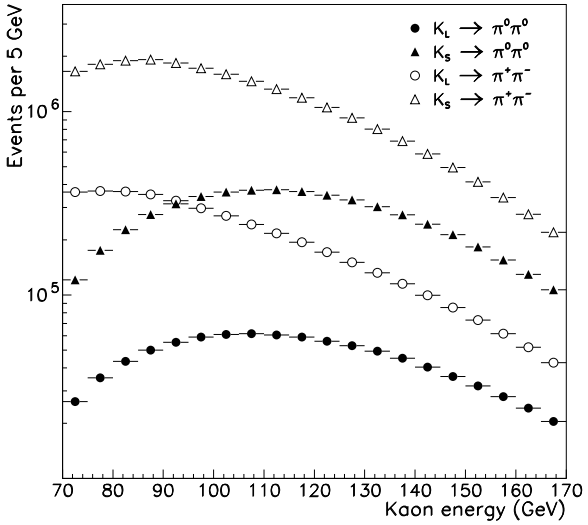

Figure 24: Energy distribution of selected events after accounting for mistagging and after proper-time weighting of K_L events.

After applying all corrections to the double ratio, the result is

$$R = (0.99098 \pm 0.00101(\text{stat}) \pm 0.00126(\text{syst})) \tag{14}$$

The stability of the result as a function of various measurement parameters was studied extensively. The double ratio as a function of the kaon energy is shown in Fig. 25. The size of the assigned systematic uncertainties was tested by varying the most important selection cuts. By changing the background-rejection cuts, even large variations of the amount of subtracted background did not cause any shift in the result greater than the estimated uncertainty on the background. Similarly, no excessive deviations of the measurement were observed by varying cuts related to the acceptance, K_S-proton tagging, uncorrelated beam activity, the decay volume and beam scattering (see Fig. 26).

Table 7: Corrections and systematic uncertainties on the double ratio. In order to obtain the effect on $\mathrm{Re}(\varepsilon'/\varepsilon)$, the numbers must be divided by a factor of 6 (Eq. 1).

		in 10^{-4}	
$\pi^+\pi^-$ trigger inefficiency		-3.6	$\pm$ 5.2
AKS inefficiency		$+1.1$	$\pm$ 0.4
Reconstruction	of $\pi^0\pi^0$	—	$\pm$ 5.8
	of $\pi^+\pi^-$	$+2.0$	$\pm$ 2.8
Background	to $\pi^0\pi^0$	-5.9	$\pm$ 2.0
	to $\pi^+\pi^-$	$+16.9$	$\pm$ 3.0
Beam scattering		-9.6	$\pm$ 2.0
Accidental tagging		$+8.3$	$\pm$ 3.4
Tagging inefficiency		—	$\pm$ 3.0
Acceptance	statistical	$+26.7$	$\pm$ 4.1
	systematic		$\pm$ 4.0
Accidental activity		—	$\pm$ 4.4
Long term variations of K_S/K_L		—	$\pm$ 0.6
Total		$+35.9$	$\pm$ 12.6

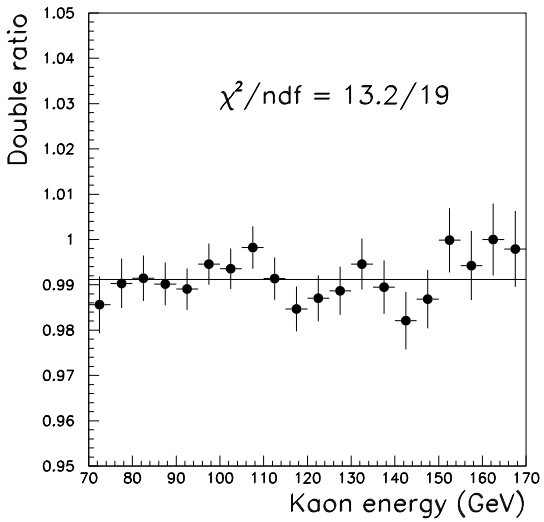

Figure 25: Corrected double ratio as a function of the kaon energy.

The stability of the result was also tested with respect to the time variation of the measurement conditions. In this context, the double ratio was measured in run periods defined by technical accelerator stops. Further checks were performed as functions of spill time, SPS revolution phase, 50 Hz mains phase, the spectrometer magnet polarity setting, and the time of day.

Another test consisted of splitting the $\pi^+\pi^-$ data sample into converging and diverging topologies, depending on the orientation of the track-charges in the magnetic field of the spectrometer, thereby selecting different acceptances and momentum resolutions. The steadiness of the drift-chamber read-out overflow rejection was tested by accepting a special class of overflow-events which affect only one pair of staggered drift chamber planes, and have only moderate effects on the trigger and reconstruction efficiencies. The variations observed in all tests are well within the assigned systematic uncertainties.

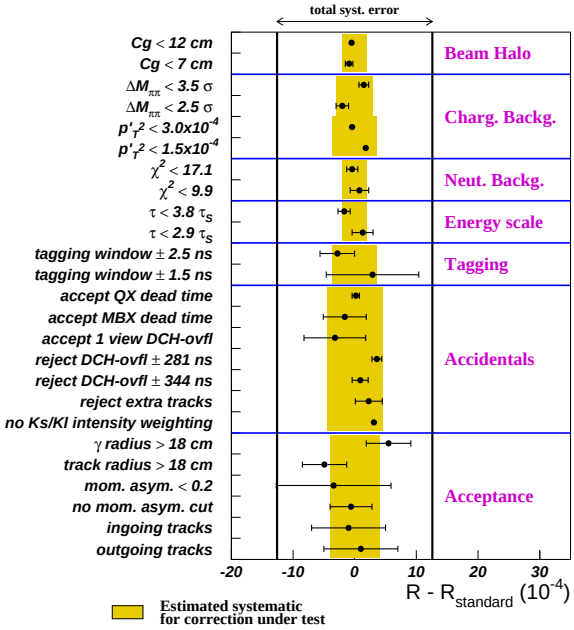

Figure 26: Stability of the double ratio with variations of the selection cuts. The grey band shows the uncertainty related to the cut concerned. $R_{\rm standard}$ represents the value from Eq. 14.

The data filtering, selection and calculation of the corrections were performed by several independent groups. One analysis adopting a different scheme of data compacting and filtering was performed in parallel to the one presented. In this analysis, several selection criteria were chosen differently, and procedures (such as the background subtraction) were conceived independently. This analysis obtained a result fully confirming the above measurement.

Converting the corrected double ratio using Eq. 1, the following measurement of the direct CP violation parameter $\mathrm{Re}(\varepsilon'/\varepsilon)$ is obtained:

$$\mathrm{Re}(\varepsilon'/\varepsilon) = (15.0 \pm 1.7(\mathrm{stat}) \pm 2.1(\mathrm{syst}))\times 10^{-4} \tag{15}$$

Adding the two uncertainties in quadrature gives:

$$\mathrm{Re}(\varepsilon'/\varepsilon) = (15.0 \pm 2.7)\times 10^{-4} \tag{16}$$

The combined NA48 $\mathrm{Re}(\varepsilon'/\varepsilon)$ measurement, including the result from the 1997 data [10], is:

$$\mathrm{Re}(\varepsilon'/\varepsilon) = (15.3 \pm 2.6)\times 10^{-4} \tag{17}$$

where correlated uncertainties are taken into account.

12 Conclusions

The NA48 measurement of the direct CP violation parameter $\mathrm{Re}(\varepsilon'/\varepsilon)$, based on the analysis of data from the 1998 and 1999 data taking periods, is in good agreement with the result from the 1997 data. The combination of both results deviates from zero by 5.9 standard deviations.

13 Acknowledgements

It is a pleasure to thank the technical staff of the participating laboratories and universities for their efforts in the design and construction of the apparatus, in the operation of the experiment, and in the processing of the data.

References

[1] J.H. Christenson et al., Phys. Rev. Lett. 13, 138 (1964)
[2] L. Wolfenstein, Phys. Rev. Lett. 13, 562 (1964).
[3] M. Kobayashi and K. Maskawa, Prog. Theor. Phys. 49, 652 (1973).
[4] M. Holder et al., Phys. Lett. B 40, 141 (1972).
M. Banner et al., Phys. Rev. Lett. 28, 1957 (1972).
[5] J. Ellis, M.K. Gaillard and D.V. Nanopoulos, Nucl. Phys. B 109, 213 (1976).
F.J. Gilman and M.B. Wise, Phys. Lett. B 83, 83 (1979).
[6] H. Burkhardt et al., Phys. Lett. B 206, 169 (1988).
[7] G. Barr et al., Phys. Lett. B 317, 233 (1993).
[8] L.K. Gibbons et al., Phys. Rev. Lett. 70, 1203 (1993).
[9] A. Alavi-Harati et al., Phys. Rev. Lett. 83, 22-27 (1999).
[10] V. Fanti et al., Phys. Lett. B 465, 335-348 (1999).
[11] M. Ciuchini, Nucl. Phys. B (Proc. Suppl) 99B, 27-34 (2001) and references therein.
[12] C. Biino et al., CERN-SL-98-033(EA) and Proceedings of 6th EPAC, Stockholm 1998, IOP, 2100-2102 (1999).
[13] N. Doble, L. Gatignon, P. Grafström, Nucl. Intr. and Methods B 119, 181 (1996).
[14] V. Fanti et al., The beam and detector for a precision CP violation experiment, NA48, to be published.
[15] P. Graftström et al., Nucl. Inst. and Methods A 344, 487 (1994).
[16] H. Bergauer et al., Nucl. Instr. and Methods A 419, 623 (1998).
[17] D. Béderède et al., Nucl. Instr. and Methods A 367, 88 (1995).
I. Augustin et al., Nucl. Instr. and Methods A 403, 472 (1998).
[18] G.D. Barr et al., Nucl. Instr. and Methods A 370, 413 (1993).
[19] B. Hallgren et al., Nucl. Instr. and Methods A 419, 680 (1998)
C. Cerri in A. Antonelli et al.(Eds) Proc. VI Int. Conf. on Calorimetry in HEP, Frascati Physics Serie 6, 1996 p. 841
G. Martin-Chassard et al. in A. Antonelli et al.(Eds) Proc. VI Int. Conf. on Calorimetry in HEP, Frascati Physics Serie 6, 1996, p.799.
[20] G. Unal for the NA48 collaboration, 9th International Conference on Calorimetry, 9-14 October 2000, Annecy France, hep-ex-0012011.
[21] R. Moore et al., Nucl. Instr. and Methods B 119, 149-155 (1996).
[22] R. Arcidiacono et al., Nucl. Inst. and Methods A 443, 20 (2000).
[23] M. Jeitler et al., Nucl. Inst. and Methods A 400, 101 (1997).
[24] G. Barr et al., The trigger for $K^0 \to \pi^0\pi^0$ decays of the NA48 experiment at CERN, to be published.
[25] S. Anvar et al., Nucl. Inst. and Methods A 419, 686 (1998).
[26] GEANT Description and Simulation Tool, CERN Program Library Long Writeup W5013 (1994).
[27] S. Palestini et al., Nucl. Instr. and Methods A 421, 75-89 (1999).
[28] E.J. Ramberg et al., Phys. Rev. Lett. 70, 2525 (1993).
[29] Particle Data Book, E.P.J, Vo 3, Nb 1-4, (1998).